

The BaLROG project - I. Quantifying the influence of bars on the kinematics of nearby galaxies

M. K. Seidel^{1,2*}, J. Falc3n-Barroso^{1,2}, I. Mart3nez-Valpuesta^{1,2}, S. D3az-Garc3a³
E. Laurikainen^{3,4}, H. Salo³, J. H. Knapen^{1,2}

¹*Instituto de Astrof3sica de Canarias, E-38200 La Laguna, Tenerife, Spain*

²*Departamento de Astrof3sica, Universidad de La Laguna, E-38205 La Laguna, Tenerife, Spain*

³*Astronomy and Space Physics, P.O. Box 3000, FI-90014 University of Oulu, Finland*

⁴*Finnish Center for Astronomy with ESO (FINCA), University of Turku, Finland*

ABSTRACT

We present the *BaLROG* (Bars in Low Redshift Optical Galaxies) sample of 16 morphologically distinct barred spirals to characterise observationally the influence of bars on nearby galaxies. Each galaxy is a mosaic of several pointings observed with the IFU spectrograph SAURON leading to a tenfold sharper spatial resolution (~ 100 pc) compared to ongoing IFU surveys. In this paper we focus on the kinematic properties. We calculate the bar strength Q_b from classical torque analysis using $3.6 \mu\text{m}$ *Spitzer* (S^4G) images, but also develop a new method based solely on the kinematics. A correlation between the two measurements is found and backed up by N-body simulations, verifying the measurement of Q_b . We find that bar strengths from ionised gas kinematics are ~ 2.5 larger than those measured from stellar kinematics and that stronger bars have enhanced influence on inner kinematic features. We detect that stellar angular momentum "dips" at 0.2 ± 0.1 bar lengths and half of our sample exhibits an anti-correlation of h_3 - stellar velocity (v/σ) in these central parts. An increased flattening of the stellar σ gradient with increasing bar strength supports the notion of bar-induced orbit mixing. These measurements set important constraints on the spatial scales, namely an increasing influence in the central regions (0.1-0.5 bar lengths), revealed by kinematic signatures due to bar-driven secular evolution in present day galaxies.

Key words: galaxies: kinematics and dynamics, galaxies: evolution, galaxies: formation, galaxies: structure, galaxies: bulges, techniques: spectroscopic

1 INTRODUCTION

The elongated shapes of bars in nearby galaxies were already identified by Hubble in the mid-30's (Hubble 1936). By the 90s, reported bar fractions reached values of $\sim 30\%$ in local galaxies, each in SBs and SABs (de Vaucouleurs et al. 1991). With the arrival of extensive imaging surveys, several works reported that at least 2/3 of the local disc galaxies exhibit bars (e.g., Knapen, Shlosman & Peletier 2000; Eskridge et al. 2000; Sheth et al. 2008), with an increasing fraction found in the infrared. Our own Galaxy was also found to host a bar (e.g. Blitz & Spergel 1991), confirmed by large spectroscopic surveys detecting prominent cylindrical rotation (e.g. BRAVA Howard et al. 2009, ARGOS Ness et al. 2013). Bars are ubiquitous in the local Universe (e.g. Eskridge et al. 2000; Knapen, Shlosman & Peletier 2000; Whyte et al. 2002; Marinova & Jogee 2007; Men3ndez-Delmestre et al. 2007; Barazza, Jogee & Marinova 2008; Aguerri, M3ndez-Abreu & Corsini 2009; M3ndez-Abreu, S3nchez-Janssen & Aguerri 2010; Masters et al.

2011; M3ndez-Abreu et al. 2014; Cisternas et al. 2014) and have even been found at higher redshifts (z) (e.g., Abraham et al. 1996; Elmegreen, Elmegreen & Hirst 2004; Jogee et al. 2004; Simmons et al. 2014), but their high- z fraction seems to be smaller than in the local Universe (e.g., Sheth et al. 2008; Nair & Abraham 2010). But how do bars form and how do they influence the evolution of a galaxy?

In the early Universe, galaxies were closer together and their evolution was dominated by interactions. Nowadays, due to the accelerating expansion of the Universe, distances between galaxies are increasing. Therefore, the internal evolution experienced by the galaxy in isolation – usually termed *secular evolution* – is increasingly important. Theoretical studies propose that bars have a great influence on this internal evolution (see, e.g., Kormendy & Kennicutt 2004 for a review). N-body simulations have helped to understand barred galaxies, their orbital structures and their influence on different galaxy properties (e.g. Combes & Sanders 1981; Athanassoula 1992a,b; Debattista & Sellwood 2000; Athanassoula 2003; Bureau & Athanassoula 2005; Martinez-Valpuesta, Shlosman & Heller 2006; Minchev & Famaey 2010; Wang et al. 2012;

* E-mail: mseidel@iac.es

Athanassoula, Machado & Rodionov 2013). Because of their significant departure from axisymmetry and the associated torques, bars are likely to play a key role in disc galaxy evolution via a number of processes: (1) redistribution of the dissipative component (as witnessed by e.g., central mass concentration, Sakamoto et al. 1999; Knapen et al. 1995, or flattening of chemical abundance gradients, Martin & Roy 1994); (2) triggered star formation, associated with bar-driven crowding and shocks (e.g. spiral arms, rings) or central gas accumulation (nuclear starbursts and AGN, e.g. Coelho & Gadotti 2011); (3) redistribution of the stellar component (e.g., Gadotti & dos Anjos 2001); (4) heating of the stellar component and build-up of bulge structures (e.g., Bureau & Freeman 1999; Chung & Bureau 2004; Fathi & Peletier 2003).

Many observational studies have investigated barred galaxies in profound detail as well as statistically and provided insights on their photometry, morphology, kinematics and stellar populations (e.g., Sheth et al. 2005; Gadotti & de Souza 2006; Laurikainen et al. 2007; Buta et al. 2010; Laurikainen et al. 2011; Pérez & Sánchez-Blázquez 2011; Sánchez-Blázquez et al. 2011, 2014; Barrera-Ballesteros et al. 2014; Kim et al. 2014). Because of the relative ease with which gas can be observed, the gas dynamics of barred galaxies are fairly well known, strongly constraining the models available (hydro, SPH, sticky particles). In contrast, the stellar component has not been studied extensively yet, so that the dynamical theories (potential and orbital structure) remain poorly tested. In particular, our study aims to perform a thorough and direct test of the increasing effect on the stellar kinematics with increasing bar strength. The consistency of bar-driven bulge formation scenarios (through gaseous inflow, recurring bar formation/destruction, recurrent buckling events or other similar mechanisms) also still needs to be understood in more detail.

One of the most important parameters in the characterisation of bars (together with properties such as bar length or pattern speed) is its "strength". Since our aim is to quantify the influence of the bar on the host galaxy, we start our study with a detailed determination of this parameter. Analysing our sample in this way, we hope to find indications of common features that will be more pronounced in more strongly barred systems. Numerous attempts have been made to define a bar strength parameter in the past, such as the bar axis ratio (e.g., Martin 1995; Martinet & Friedli 1997). Aguerri, Beckman & Prieto (1998) related the amplitude of $m = 2$ and $m = 0$ components as a measure of bar strength. In 1981, Combes & Sanders (1981) suggested a measure of bar strength, based on the maximum of the bar induced tangential force, normalised to the axisymmetric radial force field, denoted as Q_b , and widely used in observational studies (e.g., Buta & Block 2001; Laurikainen & Salo 2002; Block et al. 2004; Buta et al. 2005; Salo et al. 2010). To calculate Q_b in this study, we use the polar method (Salo et al. 1999; Laurikainen & Salo 2002).

Numerical simulations (e.g., Athanassoula 2003, 2005; Bournaud, Combes & Semelin 2005; Kim et al. 2012; Kim & Stone 2012; Łokas et al. 2014) often use comparable measurements for bar strength and find correlations of increased bar strength with increased angular momentum exchange, higher masses and velocity dispersions, but also investigate the influence of magnetic fields and dust lanes (e.g., Peebles & Martini 2006). In this paper we introduce a new method of measuring the bar strength using stellar velocity maps, based on the recent kinematic decomposition developed by Maciejewski, Emsellem & Krajnović (2012). This will provide an independent view and check of the assumptions made when computing Q_b using only the photometry.

In order to quantify the influence of bars on the properties

of their host galaxies, we present in this paper integral-field spectroscopic observations of a sample of 16 nearby barred galaxies. The panoramic field of view (FoV), which we combined to large mosaics for each galaxy, allows us to investigate these galaxies in unique detail and probe the influence of bars from the inner regions up until co-rotation. This is the first of a series of papers trying to unravel the influence of bars in detail combining this high spatial resolution dataset with recent simulations and novel analysis techniques. In this paper we will focus on the kinematics and establish a yardstick to measure the strength of the bars in order to test their influence on other parameters. In a forthcoming paper we will continue with a stellar population analysis (BaLROG II, Seidel et al. in prep.).

The paper is organised as follows. In section 2 we explain the motivation of our sample, the observations and data reduction. Section 3 summarises the methods employed, particularly explaining our calculation of the kinematic torque. We present our results in Section 4 and discuss their implications in Section 6. Our main conclusions are summarised in Section 7. Throughout the paper the cosmological parameters used are $H_0 = 67 \text{ km s}^{-1} \text{ Mpc}^{-1}$, $\Omega_\Lambda = 0.7$ and $\Omega_m = 0.3$ (Planck Collaboration et al. 2014).

2 DATA

2.1 Sample selection

The parent sample from which our target galaxies are drawn is the S⁴G survey of nearby galaxies (Sheth et al. 2010). We restricted our initial choice to barred galaxies with inclinations below 70° and brighter than $M_B = -18.0 \text{ mag}$ to ensure high quality data. As we took our sample from the S⁴G survey, we were naturally constrained to those galaxies with $cz \leq 3000 \text{ km s}^{-1}$ so that important spectral features (H β , Mg*b*) remain within the wavelength range probed by SAURON. This instrument is mounted on the William Herschel Telescope (WHT) in La Palma at the Observatorio del Roque de los Muchachos. Therefore, galaxies with sky declinations between $-2^\circ \leq \delta \leq 60^\circ$ were chosen to achieve optimal visibility. The entire exercise resulted in a large number of galaxies (~ 100), most of which were located in the vicinity of or within the Virgo Cluster. Full 2D spectroscopic analysis of a large sample was beyond our capabilities in terms of observing time. We thus carefully inspected different sets of numerical simulations and images of the S⁴G survey and selected those galaxies with prominent bars in different apparent stages of their evolution and with different morphologies. In addition, we selected both early-type and late-type galaxies and those with inclinations below 60° to reduce uncertainties (e.g. in the Q_b determination).

Our target sample consists of 16 galaxies (see Fig. 1), a number that provides a reasonable representation of different types of bars. The number of SAURON pointings greatly exceeds this number: the dataset for each galaxy is a mosaic of several pointings (up to seven individual IFU pointings) allowing us to reach the spatial detail that we aimed for while also covering the bars out to the beginning of their surrounding discs. The limitations of the size of our sample are obvious. However, while large integral field surveys such as CALIFA, SAMI or MaNGA provide large enough samples for statistics, they lack the detailed spatial sampling provided by this work (e.g. we sample at typically 100 pc, even maintained with our Voronoi-binning (within the bar region) which is in most cases at least a factor 10 better than the larger surveys). Table 1 gives the entire list of observed targets and basic properties.

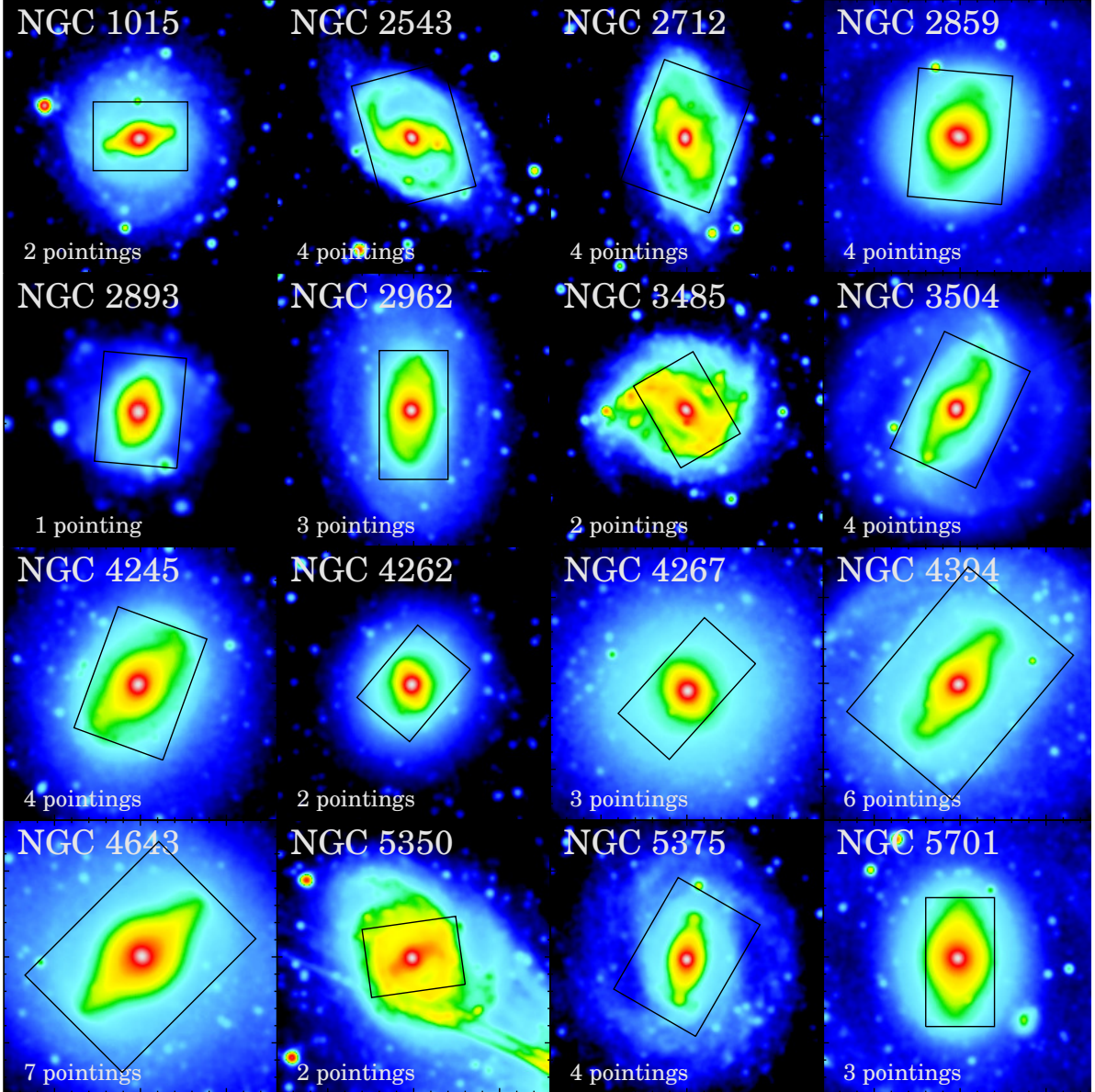


Figure 1. *Spitzer* images drawn from the S⁴G survey of nearby galaxies (Sheth et al. 2010) of our sample observed with SAURON. The number of IFU pointings is indicated in the left lower part for each galaxy. The final SAURON mosaic, composed of individual pointings of 30×40 arcsec FoV, is shown on top of the images. North is up and East is towards the left in all cases. The extensions of the S⁴G fields shown here (squares with indicated mosaic on top) are 160 × 160 arcsec, except for NGC2893 where it is only 100×100 arcsec.

2.2 Observations

The observations were carried out in four consecutive runs in March 2012, January 2013, April 2013 and January 2014 at the WHT in La Palma with the SAURON integral field unit (Bacon et al. 2001). In the employed low-resolution mode, this instrument has a field of view of 33'' × 41'', spatial sampling of 0''.94 × 0''.94 per lenslet (1431 in total) and a spectral resolution of full width at half maximum (FWHM) of 3.9 Å. Its wavelength coverage ranges from 4760 Å to 5300 Å, leading to the above mentioned redshift limitations chosen to include important emission and stellar absorption line features.

We observed up to 7 SAURON pointings per galaxy to build a large mosaic. The final maps extend along the bars up until the

start of the disc, allowing us to probe radial dependencies within and outside the bar, while also resolving great spatial detail. This strategy was quite costly in time: for the small sample of 16 galaxies we invested 54 pointings in total, each of 1–2 hours depending on the galaxy’s surface brightness. Table 2 summarises the number of pointings and the total exposure times for each galaxy. Figure 1 shows the final extent of the mosaic overlaid on top of the S⁴G images.

Apart from the large pointing offsets, we introduced small dithers within each pointing of typically 1 to 2''. This helps us to account for a couple of bad columns in the CCD and to improve our sampling. The orientation of the field of view (FoV) of SAURON was such that the 146 sky lenslets always pointed away from the

Table 1. Galaxy Sample. - (1) Galaxy name, (2) Hubble type, (3, 4) J2000 coordinates (right ascension, declination), (5) systemic velocity, (6) inclination, (7) bar length, (8) position angle, (9) bar position angle, (10) effective radius (r_e). Objects forming part of the Virgo cluster are marked with a small v next to their name. Notes. - All morphological classifications, coordinates and V_{sys} are from the *NASA Extragalactic Database (NED)*, <http://ned.ipac.caltech.edu/>. All inclinations, PAs and effective radii of the galaxy (r_e) are from the S^4G P4 (Salo et al. 2015, accepted to ApJS) while bar lengths and bar PAs are determined by Herrera-Endoqui et al. (2015, submitted) (here the ones by visual inspection).

Galaxy (1)	Hubble Type (2)	RA (hh mm ss.ss) (3)	Dec (dd mm ss.ss) (4)	V_{sys} (km s^{-1}) (5)	Inclination (deg) (6)	Bar Length (arcsec) (7)	PA (degrees) (8)	PA_{bar} (degrees) (9)	r_e (arcsec) (10)
NGC 1015	SBa	02 38 11.56	-01 19 07.3	2628	30.5	21.5	-8.3	101.4	19.73
NGC 2543	SB(s)b	08 12 57.92	+36 15 16.7	2471	59.9	14.9	37.0	105.5	26.56
NGC 2712	SBb	08 59 30.47	+44 54 50.0	1815	60.5	20.5	3.6	22.6	25.09
NGC 2859	(R)SB0 ⁺ (r)	09 24 18.53	+34 30 48.6	1687	37.2	34.4	1.8	169.6	22.41
NGC 2893	SB0-a	09 30 16.96	+29 32 23.9	1703	17.4	12.0	88.1	164.1	4.58
NGC 2962	SB0-a	09 40 53.93	+05 09 56.9	1960	49.0	30.7	8.3	172.7	20.50
NGC 3485	SBb	11 00 02.38	+14 50 29.7	1436	20.4	21.0	-64.6	40.6	26.38
NGC 3504	SBab	11 03 11.21	+27 58 21.0	1539	12.8	37.1	-41.7	148.3	11.13
NGC 4245	SB0/a(r)	12 17 36.77	+29 36 28.8	886	33.3	36.3	0.5	131.0	23.52
NGC 4262 ^v	SB0 ⁻ (s)	12 19 30.57	+14 52 39.6	1359	24.5	13.4	-6.0	26.5	5.99
NGC 4267 ^v	SB0 ⁻	12 19 45.24	+12 47 53.8	983	11.9	16.9	-27.5	34.0	21.07
NGC 4394 ^v	(R)SB(r)b	12 25 55.53	+18 12 50.6	922	30.4	41.4	-57.6	143.4	36.79
NGC 4643	SB0/a(rs)	12 43 20.14	+01 58 41.8	1330	36.8	49.9	56.0	133.3	24.22
NGC 5350	SBbc	13 53 21.63	+40 21 50.2	2321	50.3	15.2	7.9	120.8	28.06
NGC 5375	SBab	13 56 56.00	+29 09 51.7	2386	29.8	27.2	-9.4	171.1	24.35
NGC 5701	(R)SB0/a(rs)	14 39 11.08	+05 21 48.5	1505	15.2	39.0	52.0	174.9	25.97

Table 2. Summary of the observations: (1) NGC number, (2) Run number, (3) Pointing number, (4) Total exposure time, in seconds.

Galaxy (1)	Run (2)	# P (3)	T_{exp} (4)
NGC 1015	2	2	12 × 1800
NGC 2543	1,2	3	10 × 1800
NGC 2712	4	4	8 × 1800
NGC 2859	1	4	16 × 1800
NGC 2893	3	1	8 × 1800
NGC 2962	4	3	9 × 1800
NGC 3485	4	2	4 × 1800
NGC 3504	3	4	12 × 1800
NGC 4245	2	4	16 × 1800
NGC 4262	1	2	8 × 1800
NGC 4267	1	3	12 × 1800
NGC 4394	2	6	24 × 1800
NGC 4643	3	7	23 × 1800
NGC 5350	2	2	8 × 1800
NGC 5375	4	4	16 × 1800
NGC 5701	1	3	12 × 1800

galaxy's centre. They are $1.9'$ from the main FoV and thus ensure a simultaneous sky exposure during the object exposure.

We took a calibration frame using a Neon lamp before and after each science frame. Skyflats were taken at dusk and dawn, as well as continuum lamp exposures with a Tungsten lamp. For the flux calibration we observed several spectrophotometric standard stars. For further spectral calibration, we also observed a broad range of stars with different spectral types from the MILES database¹ (Sánchez-Blázquez et al. 2006).

¹ <http://miles.iac.es>

2.3 Data reduction

The reduction was performed with the available SAURON pipeline XSAURON described in detail in Bacon et al. (2001). The preprocessing of raw frames includes overscan and bias subtraction. The evaluation of dark frames showed that the dark current is negligible: less than $1 \text{ e}^- \text{ pixel}^{-1} \text{ h}^{-1}$. All frames were preprocessed in this same way. After that, a model mask was created to extract the spectra. This mask builds a table indicating corresponding positions by relating the pixels on the CCD to their associated wavelengths and lenslets. The outcome is a set of three-dimensional data cubes (α , δ , λ). Wavelength calibration was achieved with the arc (neon) lamp exposures. A cross-correlation function between the neon frames taken before and after the science exposure and the one of the extraction mask defines potential slight offsets between the science frame and the mask. This analysis is based on 11 emission lines which can be seen in the wavelength range of SAURON.

The flat-fields were created with a combination of twilight and continuum lamp (tungsten) exposures. The former calibrates the spatial component, while the latter is responsible for the spectral coordinates. We used for each run a representative twilight and continuum flat exposure investigating counts and distributions of all flat exposures. On a case-by-case basis, we also chose night-dependent flats, but for the vast majority and thanks to our bright objects, the former method proved to work well. Cosmic rays were removed before the sky subtraction, where the median of the 146 dedicate sky lenslet values was computed and subtracted from the science frame spectra. Flux calibration was done using the spectrophotometric standards. Their flux correction curve was extracted comparing the observed curve with a reference spectrum. The resulting correction curve was used to calibrate all science frames. The merging and mosaicking of the individual data cubes was achieved with the XSAURON software using the integrated intensity contours in comparison with those of a g -band SDSS image. The entire mosaic was constructed with the obtained offsets and scalings between each image.

2.4 S⁴G data

We complement our SAURON mosaics with *Spitzer* 3.6 μ m images from the S⁴G (Sheth et al. 2010). As the *Spitzer* images are very deep, the outer isophotes are typically close to or beyond the $3.6 = 25.5$ mag/arcsec² in the AB magnitude system, the position angles (PA) and ellipticities (ℓ) are taken from the S4G pipeline 4 (Salo et al. 2015, accepted to ApJ). Global galaxy parameters such as the effective radii of the galaxies (r_e) are from Muñoz-Mateos et al. (2015, submitted) and the barlength measurements are from Herrera-Endoqui et al. (2015, submitted). In addition, we used the *Spitzer* images to compute bar strengths for our sample as described in Section 3.3.1. The Q_b measurements for the complete S⁴G are given in Díaz-García et al. (2015, submitted).

3 METHODS

A detailed analysis of the stellar and gas kinematics requires a minimum signal-to-noise ratio (S/N) (e.g., van der Marel & Franx 1993). We adopted the Voronoi binning scheme of Cappellari & Copin (2003) and applied it to our data to reach a minimum S/N \approx 40 per pixel for all galaxies. The central spectra remained unbinned in all cases and exceeded this S/N level (e.g. S/N>100) while in the barred regions, we reach a typical S/N of . While a S/N of 40 ensures high-quality spectra for the extraction of the mean stellar velocity, velocity dispersion as well as Gauss-Hermite moments h_3 and h_4 , it is also low enough to preserve the spatial substructures in the galaxies, as seen in the resulting maps (see Appendix C). Before we binned, we also ensured that we would not contaminate our measurements by poor quality spaxels. Therefore we excluded those spaxels with a S/N below 3 and then limited the data to an isophote with at least this average S/N level. The resulting extensions of the maps are hence due to the combined mosaic and this additional S/N minimum threshold.

3.1 Stellar kinematics

We extracted the stellar kinematics using the pPXF – penalized pixel fitting – code developed by Cappellari & Emsellem (2004). The routine fits each galaxy spectrum with a combination of template spectra from a given library. Here we use a subset of Medium-resolution Isaac Newton Telescope library of empirical spectra (MILES; Sánchez-Blázquez et al. 2006) single stellar population (SSP) model spectra (Vazdekis et al. 2010) with a range of ages and metallicities of 0.1 Gyr to 17.8 Gyr and $-0.40 < [Z/H] < +0.22$, respectively. Their mean resolution is of FWHM = 2.51 Å (Falcón-Barroso et al. 2011) and before the fitting process, we matched the spectral resolution of the models to that of our data. Throughout this work we assume a Kroupa initial mass function (IMF, Kroupa 2001). The result of pPXF is a line-of-sight velocity distribution (LOSVD) described by a Gauss-Hermite parametrisation (Gerhard 1993; van der Marel & Franx 1993) allowing the measurement of the velocity (V), velocity dispersion (σ) and higher order Gauss-Hermite moments (h_3 and h_4). From the stellar velocity and velocity dispersion, we also calculated the value of the specific stellar angular momentum λ_R (Emsellem et al. 2007), radially but also integrated within $1 r_e$. Using the code developed by Maciejewski, Emsellem & Krajnović (2012), we furthermore obtained the radial and tangential velocities V_r and V_t for a subset of our sample (see Section 3.3.2 for more details).

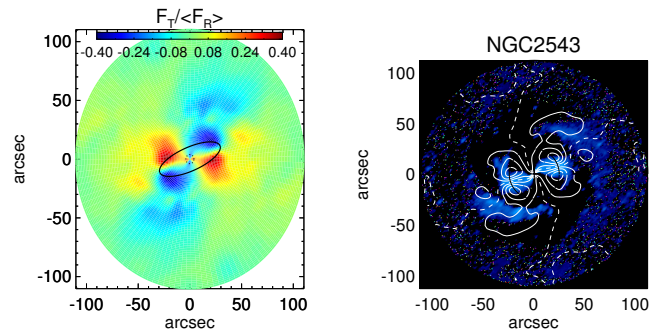


Figure 2. *Left panel:* Gravitational torque map of NGC 2543 derived from *Spitzer* image using only even Fourier components. In the top of the panel a colour bar shows the maximum and minimum Q_G ; Bar length and ellipticity are traced with a black solid line; The inner dotted circle corresponds to the S⁴G Pipeline 4 r_e of the bulge. *Right panel:* Fourier smoothed density with the axisymmetric component ($m = 0$) subtracted; Contours of equal Q_G are overplotted in white; The dotted lines indicate the regions where the tangential forces change sign.

3.2 Emission lines

We used the Gas AND Absorption Line Fitting (GANDALF) package by Sarzi et al. (2006) and Falcón-Barroso et al. (2006) to determine the ionised-gas distribution and kinematics. The code treats the emission lines as additional Gaussian templates on top of the stellar continuum and iteratively searches for the best match of their velocities and velocity dispersions. The SAURON wavelength range allows us to measure the emission line of H β λ 4861 and the doublets [OIII] λ 4959, 5007 and [NI] λ 5200, 5202 Å. We tied spectral lines kinematically to the [OIII] doublet to lower the number of free parameters given to GANDALF. We checked that leaving them free resulted in a consistent outcome. Furthermore, we imposed known relative flux relations to constrain the freedom of the doublet lines during the fitting process, namely $F([\text{OIII}]_{4959}) = 0.350 \cdot F([\text{OIII}]_{5007})$.

We will use the results from GANDALF to *clean* the spectra and produce emission-line-free datacubes for our stellar population analysis, to be presented in our Paper II.

3.3 Bar strength measurements

Bar strengths have been measured in many different ways (see introduction for details). For our analysis we will concentrate on the following two methods: (1) the photometric torque Q_b taking advantage of the S⁴G data and (2) a new measurement based on the stellar velocity maps which does not include strong model assumptions (Q_{kin}).

3.3.1 Photometric torque using 3.6 μ m *Spitzer* imaging (Q_b)

We calculated the gravitational potential of our galaxies from the 3.6 micron images, using the NIRQB code (Laurikainen & Salo 2002) based on the polar method developed in Salo et al. (1999). Before applying the Fourier transformation, the *Spitzer* images are rectified to face-on. Then, the even Fourier components (up to 20) of the surface density $I(r, \phi)$ are calculated within a polar grid. The gravitational potential $\Phi_m(r, \phi)$ is then inferred from the smoothed surface densities by applying a fast Fourier transformation in the azimuthal direction in combination with a direct summation over radial and vertical directions. We use a polar grid with 128 bins in

the azimuthal direction, which determines an angle step-size for the azimuthal Fourier transform of $2\pi/128 = 2.8^\circ$.

The calculation of the potential is based on the following assumptions:

- (i) The mass-to-light ratio is constant.
- (ii) The disc vertical scale height h_z is constant.
- (iii) The disc has an exponential vertical density distribution:

$$\rho_z(z) = \frac{1}{2h_z} \exp(-|z/h_z|). \quad (1)$$

(iv) The vertical scale height of the disc scales with the disc size as $h_z = 0.1 r_{k20}$, where r_{k20} is the 2MASS (Skrutskie et al. 2006) K -band surface brightness isophote of 20 mag arcsec $^{-2}$.

Tangential forces ($F_T(r, \phi) = \frac{1}{r} \partial \Phi(r, \phi) / \partial \phi$) and radial forces ($F_R(r, \phi) = \partial \Phi(r, \phi) / \partial r$) are obtained via integration. Non-axisymmetric forces in the galaxy are characterised by the ratio of the tangential force to the mean axisymmetric radial force field:

$$Q_G(r, \phi) = F_T(r, \phi) / \langle F_R(r) \rangle, \quad (2)$$

where $\langle F_R(r) \rangle$ is the azimuthally averaged radial force at a radial distance r . $Q_G(r, \phi)$ values are used to construct the gravitational torque maps of our galaxies (see example in Fig. 2). Typically, barred galaxies show a well-defined four-quadrant Q_G map, resembling a *butterfly pattern*, which is roughly symmetric with respect to the bar major axis. We take the even Fourier components uniquely (focusing on bi-symmetric structures) and we symmetrise our maps, reducing in this way the impact of sharp density clumps.

Based on the torque maps, and given a certain radial distance r and quadrant q , one can identify a maximum $Q_T(r)^q = \max(Q_G(r, \phi)^q)$. We calculate the radial profile of the relative strength of the non-axisymmetric perturbations throughout the galaxy, $Q_T(r)$, taking the mean of these four maxima. For additional information about the method, see Salo et al. (2010). Finally, the gravitational torque parameter (Q_b) corresponds to the maximum value of Q_T at the bar region.

The main source of uncertainty ($\approx 15\%$) is the poorly known vertical thickness: to account for this we have used different disc thicknesses in the calculation of the gravitational field. A small systematic error is produced by the omission of the dark halo contribution on the radial forces, but this is likely to be smaller than that associated with the vertical thickness (Díaz-García et al., submitted.)

3.3.2 Kinematic torque (Q_{kin})

In order to perform a model-independent measurement and to test the torque measure of Q_b , we developed a new method solely using the kinematics, resulting in a new parameter which we call the kinematic torque Q_{kin} . The basis of this analysis is the stellar velocity field. Using this map, we extracted the radial and tangential velocities following Maciejewski, Emsellem & Krajnović (2012), using their equations 9 and 10. This method is based on assuming a thin disc geometry to obtain the two velocity components in the equatorial plane. Further assumptions in deriving these two quantities are:

- (i) A steady state bar, hence not in buckling phases or alike.
- (ii) A symmetric bar with respect to its major axis.
- (iii) A thin galaxy disc resulting in only two velocity components.

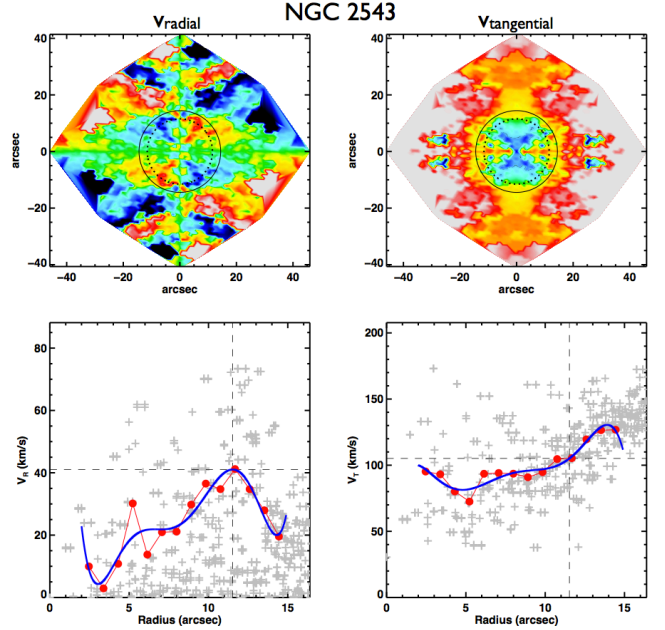


Figure 3. Radial and tangential velocities for NGC 2543. *Upper left:* radial velocity field, *upper right:* tangential velocity field; in both of them, the continuous circle indicates the bar radius and the dotted circle the radius where we measured the kinematic torque (Q_{kin}). *Lower left:* radial velocity along the radius; *lower right:* radial distribution of the tangential velocity; in both: grey crosses represent individual measurements, red points show the obtained modulation (not a fit to the gray points - see text for details) and the blue a smoothed fit to it. The dashed lines indicate the maximum found in the radial velocity and corresponding to the same radius shown for the tangential velocity (see text for details).

As the buckling phase is only a brief evolutionary stage of the bar (e.g. Shen & Sellwood 2004; Martínez-Valpuesta, Shlosman & Heller 2006), it is much more likely to observe bars in their steady state. Under the presence of spiral structure, the bar will lose its symmetry with respect to the major axis, but only at the very edges of the bar. An aspect to consider is that prominent bulges will break the third assumption in the inner regions of the bar. Following these limitations, one can conclude that the most reliable region is within the middle of the radial extension of the bar, where we expect to measure the strongest radial velocities and corresponding torques, as outlined below. In addition to these assumptions, the technique developed by Maciejewski, Emsellem & Krajnović (2012) requires the knowledge of the systemic velocity, galaxy inclination, position angle of the line-of-nodes, the bar position angle and bar length. We estimated those from the literature and close inspection of our own datasets. Furthermore, we rectified our maps to face-on in order to apply the technique.

Using the extracted radial and tangential velocities, we defined a new parameter (Q_{kin}) that measures the torque directly from the observed kinematics:

$$Q_{kin} = \frac{\max(v_{rad}(R))}{\langle \text{abs}(v_{tan,R}) \rangle}, \quad (3)$$

where we first find the radial position of the maximum value of the radial velocity (v_{rad}), and then determine the corresponding tangential velocity (v_{tan}) as the mean value in a ring around this radius. This relation is constructed analogous to the calculation of Q_b based on the fact that v_{rad} is proportional to $F_T / F_R \times v_{rot}$ and

v_{tan} roughly equal to v_{rot} . Therefore $v_{\text{rad}}/v_{\text{tan}}$ is expected to be proportional to $F_{\text{T}}/F_{\text{R}}$ (note that the ratios do not have to be equal, but only proportional). Figure 3 shows the radial (left) and tangential (right) velocity maps (top) and radial (bottom) distribution for NGC 2543 as an example. The position of the maximal radial velocity is found by evaluating the radial velocity field in rings. We expect a certain velocity modulation when tracing a circle through the four quadrants, i.e., combination of sine and cosine curve when tracing the radial velocity in a ring. This additional aspect helps us to detect and correct for outliers, i.e., unreal peaks or drops of extremely high or low values, which appear more often in the kinematic data due to higher noise levels. Hence, we avoid to simply measure the maximum which would lead to an incorrect result. A smooth version is then obtained by fitting a polynomial. In the bottom panels, we show the curves obtained when measuring the amplitudes of the modulation (red and smoothed fit in blue) compared to the individual data points (grey). It is obvious that there is a significant scatter among the individual points, but nevertheless a clear maximum can be distinguished in the radial velocity profile which is well captured with the modulation.

To further constrain the measurement, we evaluated Q_{kin} within the bar region as determined from the S^4G images. This is to avoid choosing areas where high values appear, either due to higher noise levels towards lower surface brightness areas, or due to spiral arms. In the example shown in the figure, the strength of the spiral arms can clearly be seen: in a central ≈ 20 arcsec radius, we detect the signature of the bar, but further out, the field does not become flat but shows other maxima and minima due to the torques exerted by the spiral arms. Those strong, outer values detected in the radial velocity – and thus the measured torque – is not due to the bar but to the spiral arms in this galaxy. Similar enhancements can also be seen in Fig. 2 for the computation of Q_{b} .

As the value of Q_{kin} depends on the input parameters to determine radial and tangential velocities, we chose to determine its uncertainty via a set of Monte-Carlo simulations. For each realisation, we chose a random combination of initial values of the inclination, line of nodes position angle, bar position angle and bar length, all within their uncertainties. As inclination is the most difficult to determine, we allowed an uncertainty of $\pm 10^\circ$, whereas we chose $\pm 5^\circ$ for the other parameters, leading to an overall uncertainty found in Tab. 3. Higher values would result in simply higher uncertainties in the measured torques.

Unfortunately, the determination of Q_{kin} is only possible when the kinematic major axis and the bar position angle are neither perpendicular nor parallel (at least 5° off, while an angle of 45° would be ideal). It is only under those circumstances that the method of Maciejewski, Emsellem & Krajnović (2012) can be applied to compute the required V_{rad} and V_{tan} . From the 16 galaxies in our sample, we could only measure the kinematic torque (Q_{kin}) on the following 10 systems: NGC 2543, NGC 2712, NGC 2859, NGC 2962, NGC 3504, NGC 4245, NGC 4262, NGC 4394, NGC 5350 and NGC 5701. Results are summarised in Tab. 3.

4 OBSERVED KINEMATIC PROPERTIES

This section summarises the different parameters extracted from the kinematic maps of stellar and ionised gas component. Figure 4 presents two examples of absorption-line stellar velocity maps and associated radial profiles along the major and minor axis for two galaxies in our sample, NGC 4643 (early-type) and NGC 4394 (late-type). The complete set of kinematic maps, including ionised

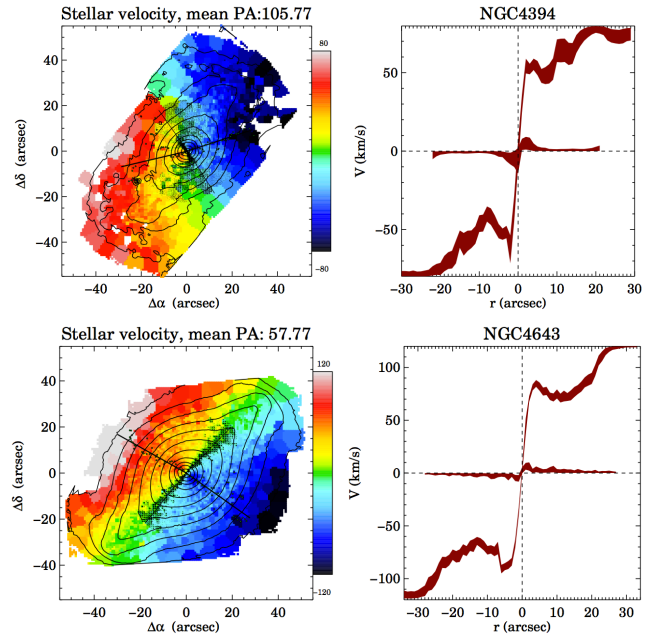


Figure 4. Stellar velocity maps and their associated major axis profile for two galaxies. The colour bars on the side each indicate the range of the parameter measured. The isophotes shown are derived from the SAURON cube reconstructed intensities and are equally spaced in steps of 0.5 magnitudes. The kinematic position angle, based on Barrera-Ballesteros et al. (2014), is given on the top. The dots indicate the bins used for determining that angle. The black lines indicate the photometric position angle, even better seen in the following figures, not demonstrating the method.

gas kinematics and Gauss-Hermite moments h_3 and h_4 are collected in Appendix C. Overlaid in all maps, we show the isophotes of the surface brightness (in $\text{mag}/\text{arcsec}^2$ with an arbitrary zero point) reconstructed from the SAURON datacubes and equally spaced in intervals of 0.5 magnitudes. In this section, we concentrate on an overview of the general kinematic trends observed in our sample. We also present the bar strength measurements from these kinematics (Q_{kin}), in comparison with the ones derived from the S^4G imaging (Q_{b}).

4.1 Stellar and gas kinematics

We investigate the orientation of the stellar and gas kinematics, comparing them to the bar axis, as well as to features that can be linked to bar-driven secular evolution. We use the entire maps as well as cuts along different axes to better unravel certain features.

A first glance at the maps shown in Appendix C reveals that the overall rotation is not strongly affected by the bar (i.e., the kinematic major axis remains almost constant as a function of radius as determined using the method by Barrera-Ballesteros et al. 2014), implying that the bar has not changed the global rotation pattern of the galaxies. We do not detect either large velocity twists in the line-of-nodes (a kinematic feature observed in simulations). Only NGC 2712 and NGC 4394 show small deviations. The absence of this feature in our maps may be due to projection effects or simply to the limited FoV, because the twist is often visible further out, such as in NGC 936 (e.g., Maciejewski, Emsellem & Krajnović 2012).

Along the kinematic major axis, we do detect in all cases the so-called double-hump rotation curve (local inner maximum followed by a slight drop and further rise) predicted by simulations

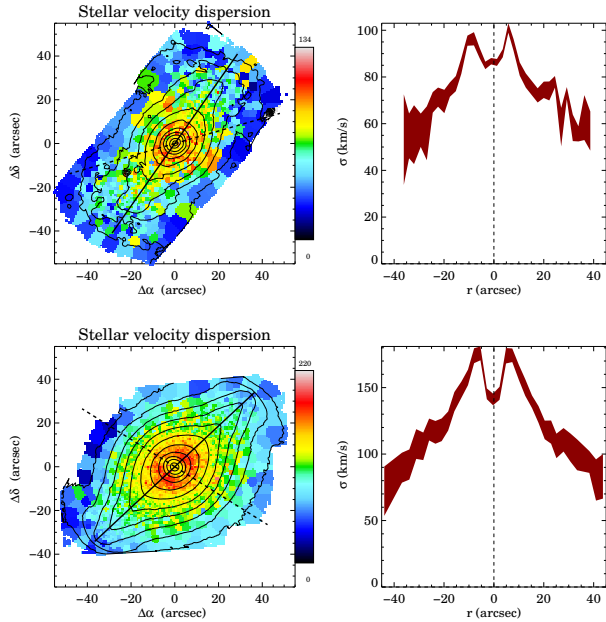


Figure 5. Stellar velocity dispersion maps and their associated profile along the bar major axis for the same two galaxies as in Fig 4. The colour bars on the side each indicate the range of the parameter measured. The continuous black line shows the bar major axis, determined from the photometry of *Spitzer* images while the dashed line indicates the global photometric position angle found previously.

(Bureau & Athanassoula 2005), so far mainly confirmed in edge-on systems (e.g., Chung & Bureau 2004). This feature can be seen in the stellar velocity maps as an enhanced area of high (low) velocity values on both sides of the nucleus, but is obviously more apparent in the radial profiles. This double-hump is clearly visible in more than 60% of the galaxies in our sample and hints towards the existence of inner discs or rings. Along the minor kinematic axis, we also find a similar distortion in the very central parts, visible as a small-scale wiggle in the minor axis rotation profile. This profile is normally expected to be flat with a value around zero, but it appears to be present for all cases. This small feature might indicate a non-perfect estimation of the global photometric position angle of the galaxies.

The stellar velocity dispersion maps, and radial profiles, of the two example galaxies NGC 4643 and NGC 4394 are presented in Fig. 5. The maps show the presence of σ -drops, a kinematic feature also predicted by simulations of barred galaxies (e.g., Wozniak et al. 2003). The fraction of galaxies in our sample that show this behaviour is 62.5%. The early types in our sample show a larger region of overall higher σ than the late types, as expected from the presence of larger central bulge structures. Peak velocity dispersion values range between 100 km s^{-1} and 220 km s^{-1} .

The corresponding kinematic maps (velocity and velocity dispersion) for the ionised gas are shown in Fig. 6 for the two example galaxies, illustrating their difference to the stellar kinematics. The ionised gas maps of the entire sample appear in general less regular with a more patchy distribution, reflecting the gas properties. We do not find gas equally distributed in all the galaxies. The absolute values of minimal and maximal rotation are generally slightly higher for the gas than for the stars in all galaxies. The kinematic major axis of the gas velocity field has the same orientation as the stellar velocity field. Only one galaxy shows a significant

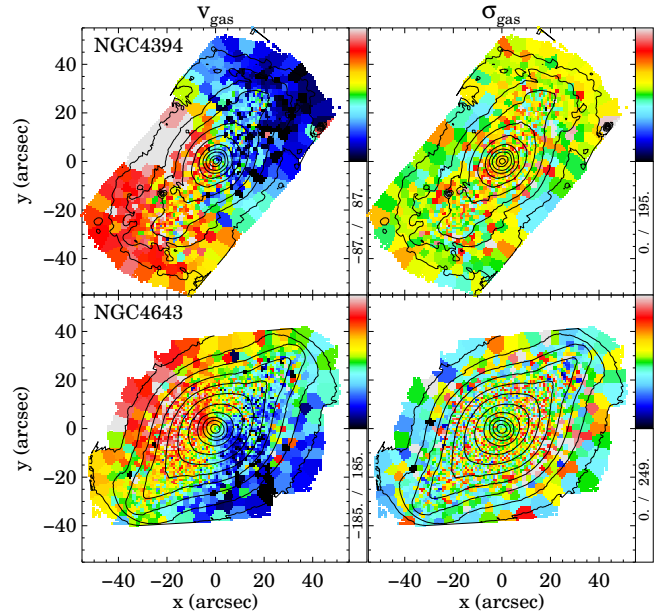


Figure 6. Velocity and velocity dispersion maps of the ionised gas component for the two examples in the BaLROG sample of galaxies.

change in orientation, NGC 4262, whereas two others (NGC 2962 and NGC 5701) show very mild differences only. Previous studies suggest that NGC 4262 might have been involved in an interaction (Vollmer, Huchtmeier & van Driel 2005). The gas velocity fields also present the double-hump feature, in some cases significantly more pronounced than in the stellar maps (e.g. NGC 3504). This confirms that the gas is more susceptible to bar-driven processes (e.g., Schwarz 1981; Ellison et al. 2011; Athanassoula, Machado & Rodionov 2013). The ionised gas velocity dispersion differs significantly from the stellar σ . It does not show a central elevation (tracing the bulge component) but exhibits slightly higher values throughout the area inside the bar isophotes. However, the pattern is extremely patchy and we lack enough coverage of the disc for a fair comparison between the morphological components. Especially in the late-type systems, some regions display higher velocity dispersion in the gas than in the stars. These are typically associated with spiral arms (e.g. NGC 3504, NGC 4394).

We will link the investigated features to the strength of the bars in Sec. 5.2.

4.2 Gauss-Hermite moments: h_3 and h_4

In addition to the first and second moment of the LOSVD distribution (V , σ), we measured the h_3 and h_4 Gauss-Hermite moments. They help to understand the distribution of orbits along the line-of-sight and can be used to distinguish dynamically distinct regions and thus indicate whether bars influence their formation.

Mathematically, h_3 measures the skewness of the LOSVD, i.e., wings on either side of the peak deviating from the otherwise Gaussian profile, while h_4 is a measurement of the kurtosis (e.g. van der Marel & Franx 1993). Within our sample, we find a large variety in those maps and just by visual inspection, we cannot identify a systematic pattern which could be attributed to the bars of their host galaxies.

Figure 7 shows the two Gauss-Hermite moments h_3 and h_4 for NGC 4394 and NGC 4643. In the first galaxy, the maps appear more uniform than in the second one, which does exhibit low-

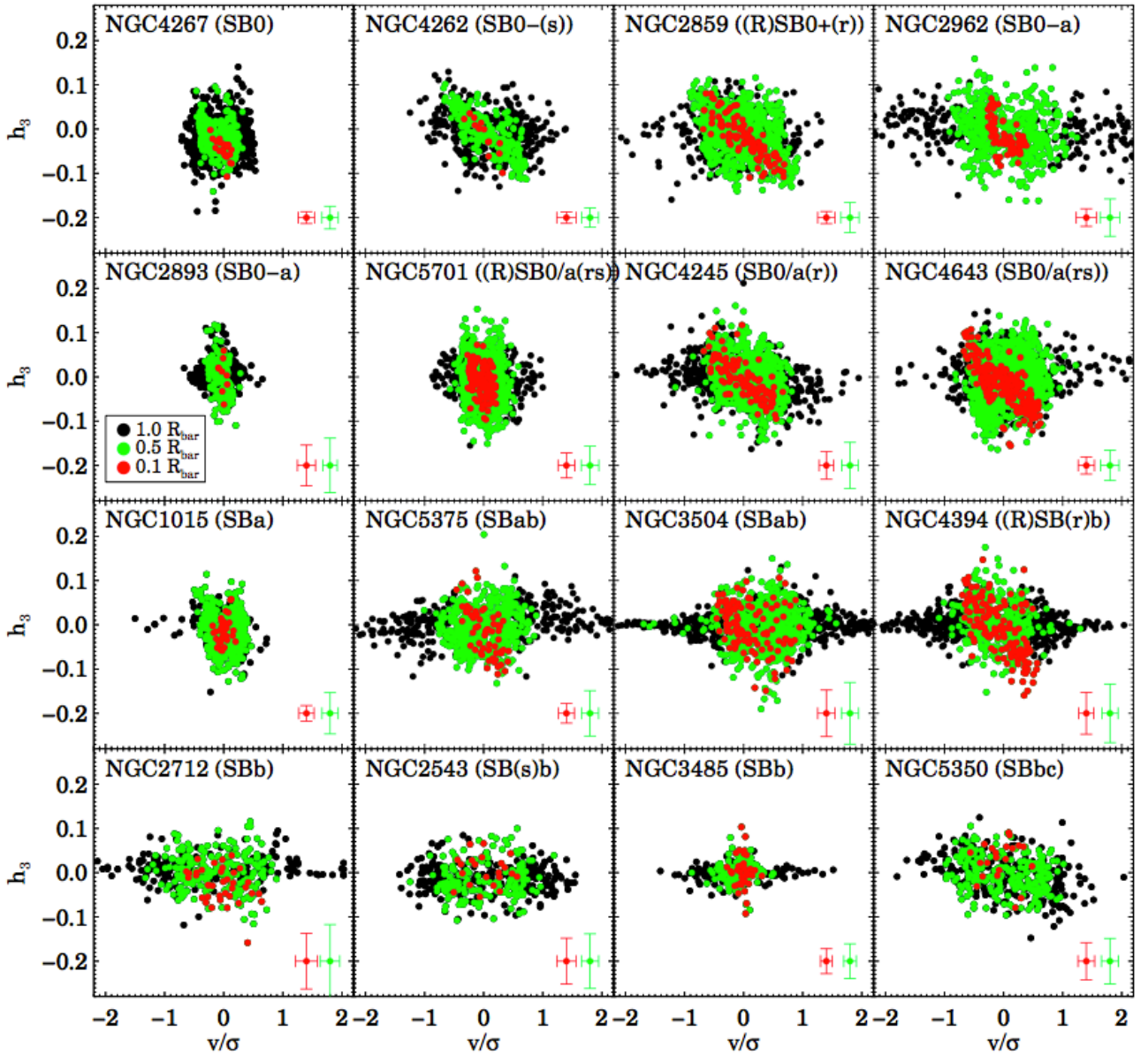


Figure 8. Individual Voronoi-binned values of h_3 versus the stellar velocity over the stellar velocity dispersion, within $1 R_{bar}$, $0.5 R_{bar}$ and $0.1 R_{bar}$. Representative error bars for the red and green regions are indicated in the lower left corner of each panel.

level structure. However, the majority of the maps of h_3 and h_4 (see more in the appendix) show very low values (below 0.1) and are rather flat throughout the FoV. In several cases a slight anti-correlation between the h_3 moment and the stellar velocity can be seen (NGC 1015, NGC 2959, NGC 2962, NGC 4245, NGC 4262, NGC 4643 and NGC 5350), while h_4 moments correlate in most cases with the velocity dispersion. We investigated the h_4 profiles along the bar major axis for kinematic signatures of peanut-shaped bulges (e.g., Debattista et al. 2005), but could not detect any clear evidence. This is a property of mainly very low inclined galaxies with strong peanut shapes seen in the photometry, so our sample is not an ideal selection for the detection of this characteristic. So far, only a few studies (e.g., Méndez-Abreu et al. 2008, 2014) have confirmed this prediction.

In the literature, the h_3 moment is often related to the stellar

velocity and both correlations and anti-correlations are found (e.g., Bureau et al. 2004). For a more robust measure we chose to correlate h_3 with V/σ , shown in Fig. 8, in order to compensate for different masses. However, we checked the relation correlating with the stellar velocity alone and did find very similar results. In the figure, Voronoi-binned values within the bar length are shown in black, within 0.5 times the bar length in green and within 0.1 times the bar length in red. There is no clear (anti-)correlation for the full extent of the bar length (nor for the effective radius, which we tested for comparison, but which is not shown here). However, the more central the aperture, the stronger the anti-correlation for about 50% of our sample, clearly depicted by the red points. The other $\sim 50\%$ of our sample do not show any (anti-)correlation at all, but a simple spread of h_3 values around zero. This behaviour is consistent across both measures – bar length or the effective radius – with the excep-

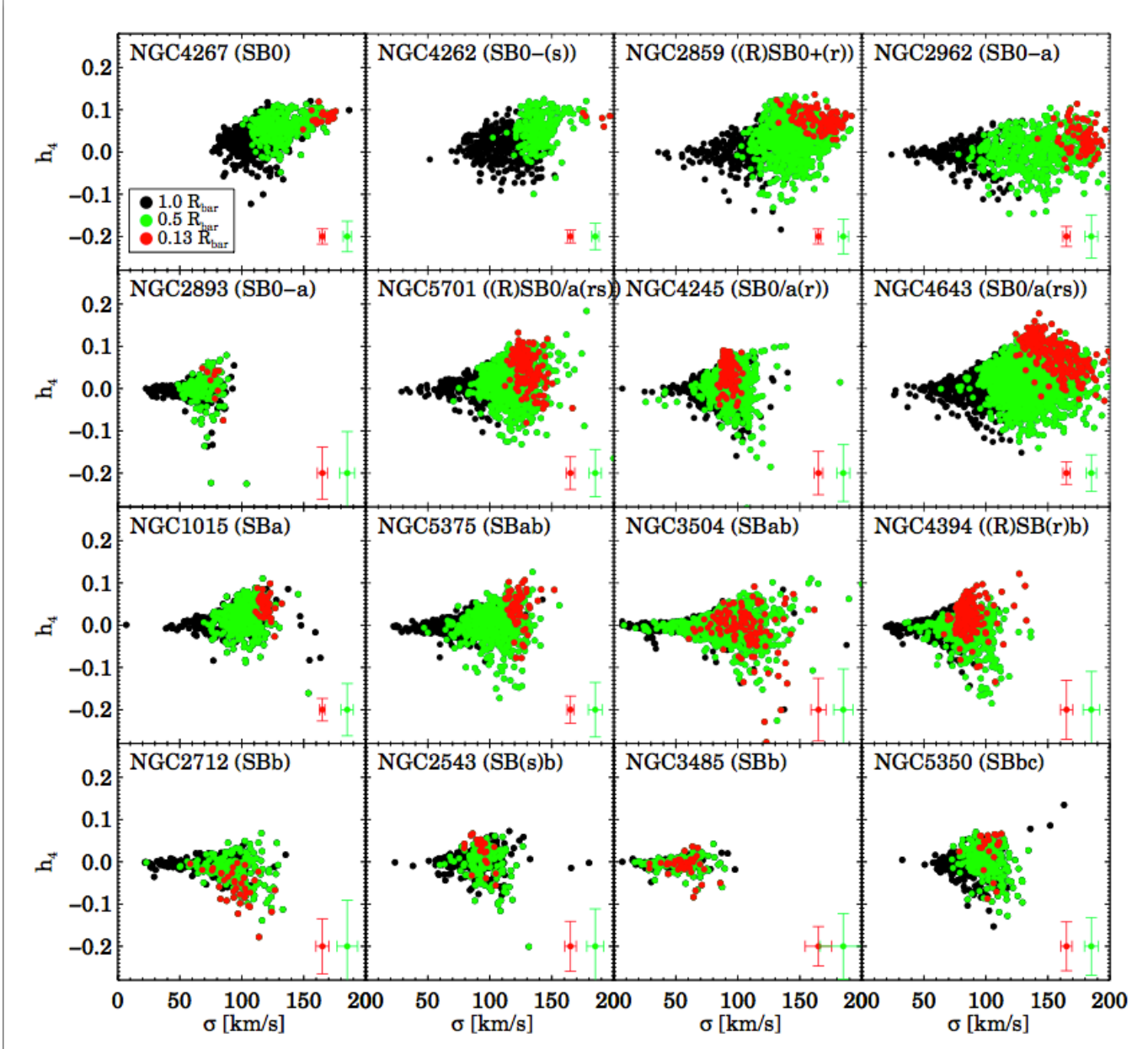


Figure 9. Individual Voronoi-binned values of h_4 versus the stellar velocity dispersion, within $1 R_{\text{bar}}$, $0.5 R_{\text{bar}}$ and $0.1 R_{\text{bar}}$. Representative error bars for the red and green regions are indicated in the lower left corner of each panel.

tion of NGC 4262. The effective radius for this galaxy is significantly smaller and captures the inner part only. Hence, as smaller apertures decreased the scatter if an anti-correlation was present, it stands out better for the effective radius measurement. In many of the other galaxies the effective radius is comparable to the bar length or at least not less than half its size. Overall, we cannot detect a tendency between late or early types, because both late types (e.g. NGC 4394) and early types (e.g. NGC 2859) show the above described behaviour, although with a mild bias towards earlier types showing stronger correlations. In the figure, we ordered the galaxies according to their Hubble type (SB0 top left to SBbc bottom right) and one can appreciate the larger scatter also amongst the innermost (red) points in the bottom row (latest types of our sample). The fact that there is no striking difference though might mean that the Hubble type is not the crucial factor, neither the bar, but the presence of

significant substructures. More than 50% of those with strong central anti-correlations have confirmed substructures such as nuclear rings, nuclear lenses or nuclear ring or bar lenses (see classifications by Laurikainen et al. 2011 and Buta et al. 2015).

The influence of bars on building up a central component is supported by this h_3 - V anti-correlation in the centres of about 50% of our sample of galaxies. Earlier studies have found a correlation as well as anti-correlation between the stellar velocity and h_3 moment, depending on the area and type of galaxy sampled. In edge-on barred galaxies, Bureau et al. (2004) and Bureau & Athanassoula (2005) detected an h_3 - V correlation over the projected bar length, expected for a thick bar. In the centres, however, they also found an anti-correlation in more than 60% of the galaxies. This can indicate the presence of multiple components with different kinematics. Hence a significant number of barred galaxies, not only in edge-

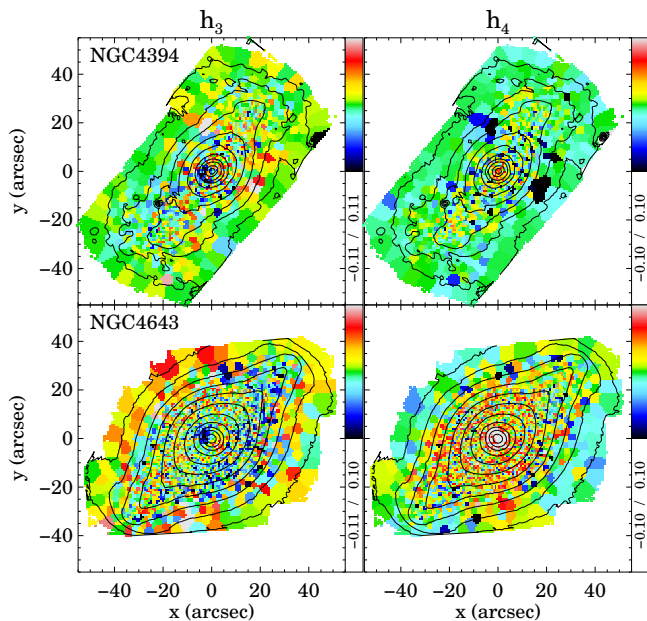


Figure 7. Gauss-Hermite maps of the stellar component for the two examples in the BaLRoG sample of galaxies.

on systems but also in our sample of different inclinations, show the presence of cold and dense (quasi-)axisymmetric central stellar discs. This supports the scenario of the bar driving gas towards the centre and nourishing star formation, resulting in this additional central component. The coincidence of a steep central light profile and star-forming ionised gas discs in these same regions (e.g. Bureau & Freeman 1999) supports this theory further. Falcón-Barroso et al. (2006) also found a link between more intense star forming regions and lower gas dispersion values. However, due to our limited wavelength range, we could not account consistently for dust correction which could influence the values of h_3 , being sensitive to dust. Dust is particularly important in late-type galaxies, but the majority of our sample are early-types and no obvious dust lanes are detected in the later types.

Figure 9 shows similar measurements for h_4 . The galaxies are again ordered by Hubble type. This parameter measures the symmetric deviation from a Gaussian profile, indicating a velocity distribution which is less (or more) peaked (negative or positive values). It is expected to correlate with the velocity dispersion (van der Marel & Franx 1993), so we chose to plot it against σ . Overall, but especially for the early types, we observe elevated values in the central regions, most probably associated with the bulge. The presence of higher h_4 values together with an occasional σ -drop hints at the presence of components with more recent star formation within a classical elliptical-like bulge component (Wozniak et al. 2003; Bureau & Athanassoula 2005). In Fig. 9, this behaviour stands out even more clearly: a higher velocity dispersion is found in the centres where the red points (corresponding to most central values, i.e., within 0.1 bar lengths) also show elevated h_4 values. Later-type galaxies are clearly different. Not only does the velocity dispersion cover a larger range of values, also the h_4 values are not particularly high in the centre or even go significantly below zero (e.g. NGC 2712, NGC 3504, NGC 3485, NGC 5350, NGC 5875). The bulge in the later-type galaxies is significantly less pronounced, therefore the mixture of more components could cause this spread of h_4 values. The strongest central concentration of elevated h_4 values, at an almost constant σ and h_4 , are found in NGC 1015,

NGC 2859, NGC 2962, NGC 4262 and NGC 4267. These are not the galaxies showing the h_3 -velocity central anti-correlation, but those to have a prominent bulge component. NGC 5701 also has a large bulge, but contains confirmed nuclear spiral structure (Erwin 2004), which could contribute to the higher spread in h_4 .

In conclusion, the analysis of Gauss-Hermite moments suggests that the centers of barred galaxies (within at least half a bar length, and even more obvious within 0.1 bar lengths) host dynamically distinct components. These could have been altered by bar-driven evolution.

4.3 Angular momentum: λ_R

We calculate λ_R as a measure of rotational versus pressure support following the prescription given in Emsellem et al. (2007), as bars are meant to work as engines redistributing angular momentum amongst the different components of a galaxy. This parameter is based on the first two stellar velocity moments and the corresponding flux and is defined as

$$\lambda_R = \frac{\sum_{i=1}^{N_p} F_i R_i |V_i|}{\sum_{i=1}^{N_p} F_i R_i \sqrt{V_i^2 + \sigma_i^2}} \quad (4)$$

for two-dimensional spectroscopy, where F_i denotes the flux, R_i the circular radius, V_i the velocity and σ_i the velocity dispersion of the i th spatial bin (going to N_p bins). As outlined in Emsellem et al. (2011), it improves the characterisation of the dynamical state of a galaxy compared to the simple measure of V/σ . It shows a clear difference, especially for non-regular rotators with irregularities in their velocity fields, whilst at the same time being correlated to the specific angular momentum of the stars.

We calculated λ_R in our sample both radially (see Fig. 10) as well as within one r_e (λ_{Re} , given in Tab. 3). We normalised the radial profiles to the bar radius to test the influence of the bar on the shape of the profile. Considering the small sample size and large variety of Hubble types and bar types, it is not surprising that we recover a variety of profiles. Yet more than 70% show a dip in λ_R at around $0.2 \pm 0.1 R_{\text{bar}}$. The only galaxy which shows a clear offset of this dip is NGC 4262, where the stellar and gas velocity fields are clearly misaligned.

This feature appears to be related to the double-hump in the velocity profile (Bureau & Athanassoula 2005), in combination with the rise in σ after the σ -drop. Three galaxies (NGC 1015, NGC 2893, and NGC 5350) do not exhibit a double-hump nor a strong σ -drop. In other galaxies (NGC 2712, NGC 4267, NGC 4262, NGC 5375), the hump feature in the stellar velocity alone seems to be strong enough to produce the drop in the λ_R profile. In other cases, in particular NGC 4245, NGC 3485 and NGC 5701, the peak of the hump in the velocity profile coincides with the peak of the velocity dispersion profile (after the central drop). Thus, despite the distinct morphologies and inclinations, we observe a common behaviour and influence on the stellar kinematics. This is likely produced by the bar, since these features seem to accumulate around a similar radius related to the bar length. This feature could probably be associated to the inner Lindblad resonance (ILR) (e.g. Elmegreen 1994; Pfenniger & Norman 1990). In fact, in several of our galaxies, nuclear rings have been detected at those locations: NGC 2859 (Erwin & Sparke 2002), NGC 3504 (Buta & Crocker 1993; Elmegreen et al. 1997), NGC 4262 and NGC 4245 (Comerón et al. 2010).

We also tested the location of the dip as a function of the effective radius of the bulge and the disc scale-length (derived from

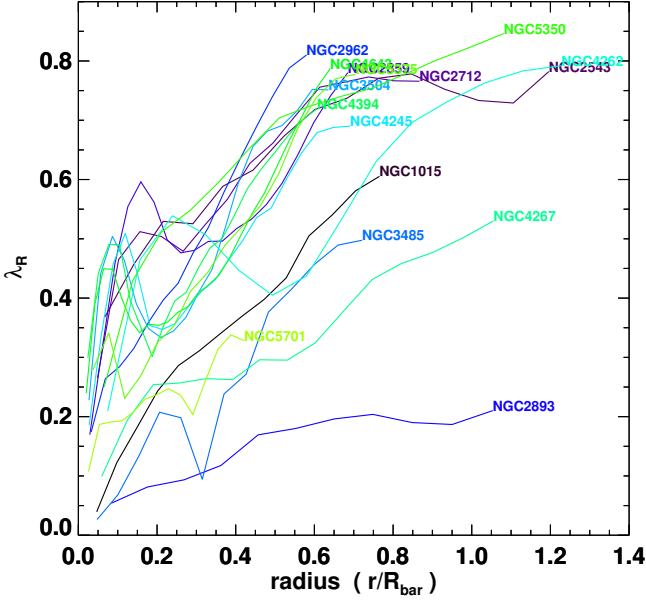


Figure 10. Radial profiles of λ_R for all galaxies, normalised to the radius of the bar. A rise and consecutive dip is observed at a similar position in the profiles of the majority of galaxies, around $0.2 \pm 0.1 R_{\text{bar}}$.

Table 3. Summary of the values obtained for λ_{R_e} and the bar strength measurements: (1) NGC number, (2) λ_{R_e} , (3) photometric torque, (4) error in the photometric torque, (5) kinematic torque, (6) error in the kinematic torque, (7) kinematic torque of the gas component, (8) error in the kinematic torque of the gas component. As the error of the measure for λ_{R_e} is negligible, we do not list it here.

Galaxy (1)	λ_{R_e} (2)	Q_b (3)	ΔQ_b (4)	Q_{kin} (5)	ΔQ_{kin} (6)	$Q_{\text{kin,g}}$ (7)	$\Delta Q_{\text{kin,g}}$ (8)
NGC 1015	0.25	0.26	0.074	-	-	-	-
NGC 2543	0.62	0.36	0.070	0.39	0.069	1.1	0.23
NGC 2712	0.65	0.28	0.044	0.37	0.044	0.46	0.07
NGC 2859	0.37	0.17	0.025	0.22	0.044	0.94	0.40
NGC 2893	0.06	0.16	0.020	-	-	-	-
NGC 2962	0.44	0.14	0.024	0.080	0.040	0.62	0.44
NGC 3485	0.52	0.38	0.064	0.33	0.084	0.84	0.43
NGC 3504	0.29	0.26	0.044	0.24	0.082	1.5	0.99
NGC 4245	0.33	0.18	0.020	0.10	0.033	0.20	0.19
NGC 4262	0.33	0.07	0.012	0.14	0.048	1.8	0.25
NGC 4267	0.24	0.04	0.013	-	-	-	-
NGC 4394	0.46	0.23	0.036	0.23	0.12	0.52	0.12
NGC 4643	0.28	0.28	0.069	-	-	-	-
NGC 5350	0.62	0.44	0.076	-	-	-	-
NGC 5375	0.47	0.23	0.044	-	-	-	-
NGC 5701	0.20	0.18	0.022	0.08	0.076	0.42	0.66

the S^4G) but did not find any correlation. This supports our suspicion that this feature is related to the bar. Similar studies have already related outer ring radii to the bar sizes (e.g., Pérez, Aguerri & Méndez-Abreu 2012) based on earlier studies and simulations (e.g. Byrd et al. 1994; Buta et al. 1995). Comerón et al. (2010) estimate that the maximal possible extension of a nuclear ring should be located at 0.25 bar lengths.

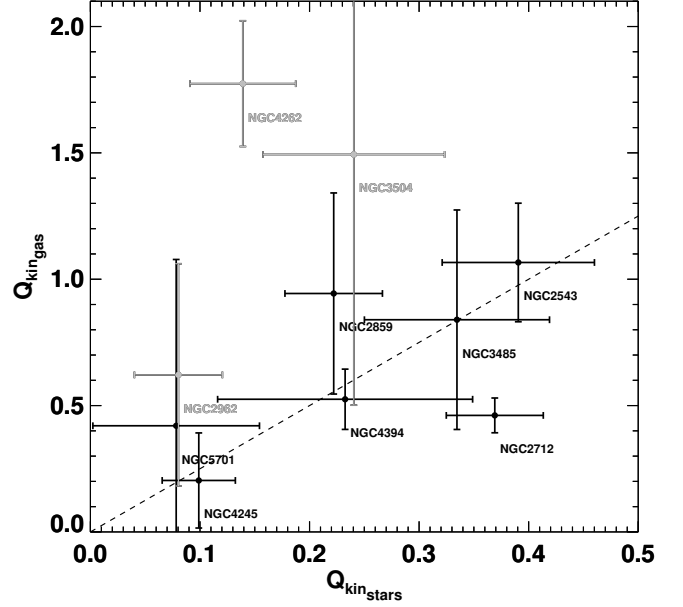


Figure 11. Kinematic gas torque versus kinematic stellar torque. The dotted line indicates a 2.5-correlation. Grey galaxies show obvious offsets between gas and stellar kinematics.

5 CONTRASTING BAR STRENGTH MEASUREMENTS

In this section we compare bar strength measurements determined according to the descriptions given in Section 3.3. For the case of Q_{kin} we additionally measure it for both the stellar and ionised-gas components. This comparison will allow us to establish the ruler that will be used in Sect. 6 to evaluate the impact of bars of different strengths on different kinematic properties of our galaxies.

5.1 Q_{kin} from stars and ionised gas

We calculated the kinematic torque (Q_{kin}) from both our stellar and ionised-gas velocity maps (values given in Tab. 3). The comparison is shown in Fig. 11. The gas is expected to respond more strongly to the bar than the stars. Overall the torque derived from the gas velocity fields is significantly higher than the stellar one. For almost all galaxies it is about 2.5 times greater than the value derived from the stellar velocity maps (dotted line). The grey points mark significantly higher values. Inspecting their gas velocity maps, we detect clear differences from the stellar velocity fields. In particular NGC 4262 shows the highest value of $Q_{\text{kin,gas}}$. The gas velocity field is counter-rotating with respect to the stellar velocity field. Therefore, a significant impact due to another process (e.g. galaxy interaction or close encounter) might be at work in this galaxy (see Vollmer, Huchtmeier & van Driel 2005). In NGC 3504, the gas velocity field shows extreme enhancements in the central regions which are not present in the stellar velocity field. It is not clear at this stage what is causing this difference. Overall, we find that the stars seem to be more stable and therefore the stellar kinematic torque agrees better with the photometric torque (see § 5.2), whereas the gas is more susceptible to other processes, leading to a larger number of outliers.

5.2 Kinematic vs photometric bar strengths

Figure 12 (top panel) compares the kinematic (Q_{kin}) versus the photometric (Q_{b}) torque measurements for the subsample of 10 galaxies, where the kinematic method was possible. Despite large uncertainties, the correlation between the two parameters is obvious. This is confirmed by a measured linear Pearson correlation coefficient of 0.83. The distribution of existing bar strengths within our limited sample is representative of larger samples of nearby galaxies (Laurikainen et al. 2004). Overall, early-type galaxies have lower values than the later types, confirming earlier results by e.g. Buta et al. (2005); Laurikainen et al. (2007). This could be a result of different factors: i) the influence of stronger spiral arms that still alter the motions within the bar region (although we tried to avoid them in our analysis), ii) the presence of more gas in later types which is more responsive to the bar could also influence the stellar motions, iii) discs in earlier types are simply hotter leading to more random versus ordered rotational motion. The dotted line in the figure indicates a one-to-one correlation.

To investigate further the relation between stellar Q_{kin} and Q_{b} , we have produced an extensive set of numerical simulations of barred galaxies following those in Martinez-Valpuesta, Shlosman & Heller (2006) and Martinez-Valpuesta & Gerhard (2011). Here we use four simulation series, I_1 , I_2 , I_3 and I_4 , each one with a different disc-to-total ratio: 0.92, 0.62, 0.43, 0.29 respectively. This setup allows us to explore the effect of distinct dark matter haloes on the torque parameters. We analysed 1800 snapshots taken at different points in time of the bar evolution. In addition, we also varied the inclination and the position angle of the bar relative to the galaxy's position angle to have different viewing angles and thus assess the influence of these parameters (see Appendix B for more details). The bar strength measurements of the simulations are presented in Fig. 12 (bottom panel).

We analysed the simulations in the same way as the observations. We calculated Q_{b} from their simulated intensity distribution and Q_{kin} from their associated stellar velocity maps (see Appendix A for details). Due to the lack of r_{K20} (k-band photometric parameter) to infer the scale height h_z (for the calculation of Q_{b}) (Speltinckx, Laurikainen & Salo 2008), we applied the de Grijs (1998) relation for intermediate type galaxies which links the scale-height to the scale-length, assuming an exponential disc without truncations. The overall trend found is consistent with what we find with the observations. Nonetheless, distinct simulation series behave systematically differently; the figure shows that higher disc fractions consistently lead to lower bar strengths, both in Q_{b} and Q_{kin} . Each simulation series exhibits low bar strengths, which correspond to snapshots in very early times in the bar formation. While I_1 soon seems to saturate and cannot grow stronger bars, the others do and saturate at later stages such that the strongest bars are found in the simulation series I_4 , the one with the highest dark matter fraction.

Given the good agreement between Q_{b} and Q_{kin} for our subset of galaxies along with the large number of simulations, we will use the photometric values determined from the S^4G images for the bar strength values, because these are available for our entire sample. Our study also serves for verifying the technique and results of Q_{b} .

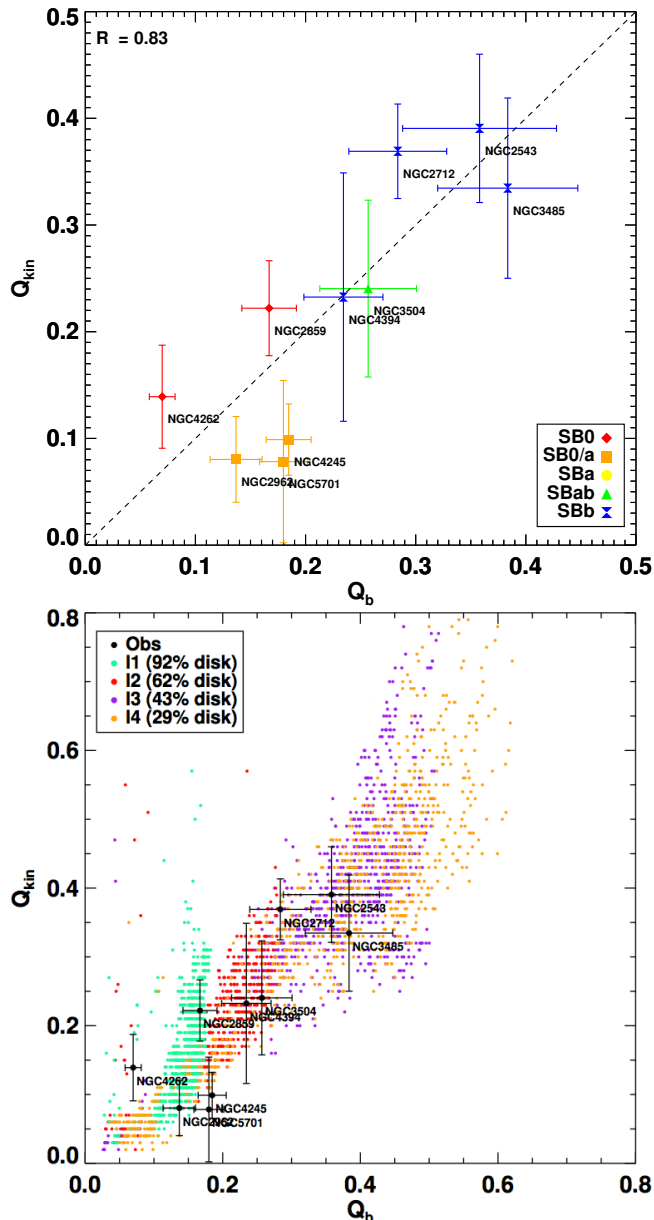


Figure 12. (Top panel) Kinematic versus photometric torque (Q_{kin} vs Q_{b}). The dotted line indicates a one-to-one correlation. Symbols are colour-coded according to Hubble type. The relation has a linear Pearson correlation coefficient of $R=0.83$. (Bottom panel) Comparison of Q_{kin} and Q_{b} for the observations (black) and the four sets of numerical simulations (I_1 , I_2 , I_3 and I_4). We only plot stages of the simulations that exclude the buckling phases.

6 THE EFFECT OF BAR STRENGTH ON GALAXY PROPERTIES

In this section we try to understand if stronger bars affect the properties of the host galaxy in a systematic way, focusing on whether it leads to stronger or weaker kinematic features.

6.1 Relation with Hubble type

Figure 13 illustrates the already observed trend of Q_{b} with Hubble type (e.g., Laurikainen et al. 2007), resulting in a linear Pearson correlation coefficient of $R = 0.96$ for our sample (averaged val-

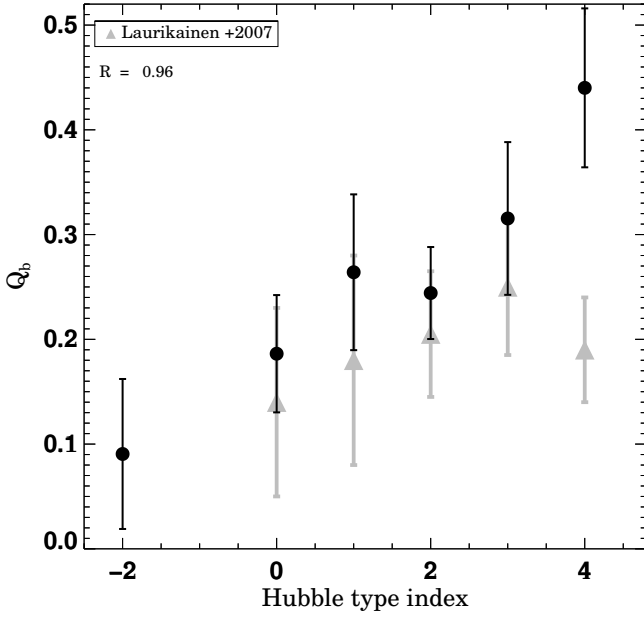


Figure 13. Bar strength as a function of Hubble type. We represent our sample averaged per Hubble type in comparison with the sample analysed in Laurikainen et al. (2007).

ues per Hubble type bin). In comparison with the observed trend found in Laurikainen et al. (2007), we cover slightly stronger bars throughout but conserving the trend, making our sample representative of rather strongly barred galaxies. For a wider study of Q_b as a function of Hubble type based on the S⁴G sample, please refer to Díaz-García (2015, submitted).

In Fig. 14 we depict the position of the dip in the λ_R profile, depicted in Fig. 10, as a function of bar strength. The dip is not observed in all galaxies, therefore we only show those, which exhibit this feature. Is this dip feature related to inner structures such as nuclear rings? We plot in gray positions of rings from the AINUR sample (Comerón et al. 2010), including three galaxies (NGC 2859, NGC 3504 and NGC 4245) that we share. Evidently, ring and dip positions do not correlate and we do not find any mathematically significant trend for either sample.

Fig. 15 shows again the position of the dip in the λ_R profile, now as a function of light concentration R_{90}/R_{50} . Apart from NGC 4262 - already found not to follow other observed trends, probably due to a recent interaction - the galaxies seem to follow a downward trend: the more concentrated the bulge, the closer is the dip feature towards the center. This could be directly related to the bulge: in our simulations with more concentrated bulges, we also find that the ILRs are located closer to the center. It could also mean that these features are more evolved in time, supporting the prediction of the migration of nuclear rings towards the center (e.g., Knapen et al. 1995; Fukuda, Habe & Wada 2000; Regan & Teuben 2003; van de Ven & Chang 2009), also recently observed by Piñol-Ferrer et al. (2014).

This trend is only mildly observed for the values of the AINUR sample, taking their measured ring radii as a comparison, because no λ_R profiles are available for that data. We further determined the position of iILR and oILR by a simple linear approximation analysing Ω -curves and estimates for the bar pattern speed. Neither the position of the dip in the λ_R profile, nor the ring radius are found at the exact same position as these resonances (in a forthcoming

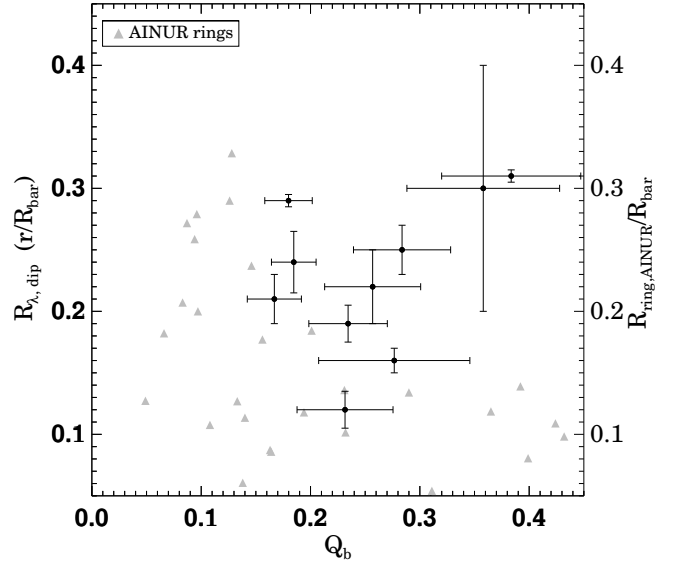


Figure 14. Position of the dip in the λ_R profile as a function of bar strength based on the profiles obtained in Fig. 10. Grey points indicate ring positions (as bar length fractions) also as functions of the bar strength, both as measured in the AINUR sample (Comerón et al. 2010).

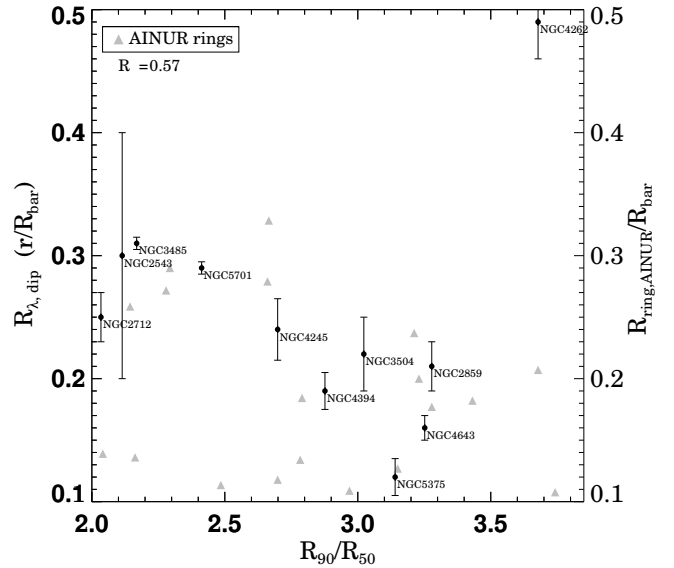


Figure 15. Position of the dip in the λ_R profile as a function of light concentration R_{90}/R_{50} based on the profiles obtained in Fig. 10. Grey points indicate ring positions (as bar length fractions) also as functions of the concentration, derived in the same way as for our sample.

paper, we will verify this by a more robust calculation of bar pattern speeds).

6.2 Influence of the bar strength on the global position angle

To quantify the influence of the bar on the global velocity map, we analysed the difference between the photometric and kinematic position angles as a function of the bar strength. We compared the photometric PA with the stellar and gas kinematic PA, as well as the difference between the stellar and gaseous components. This is shown in Fig. 16. We measured the kinematic PAs directly from the velocity maps following Barrera-Ballesteros et al. (2014).

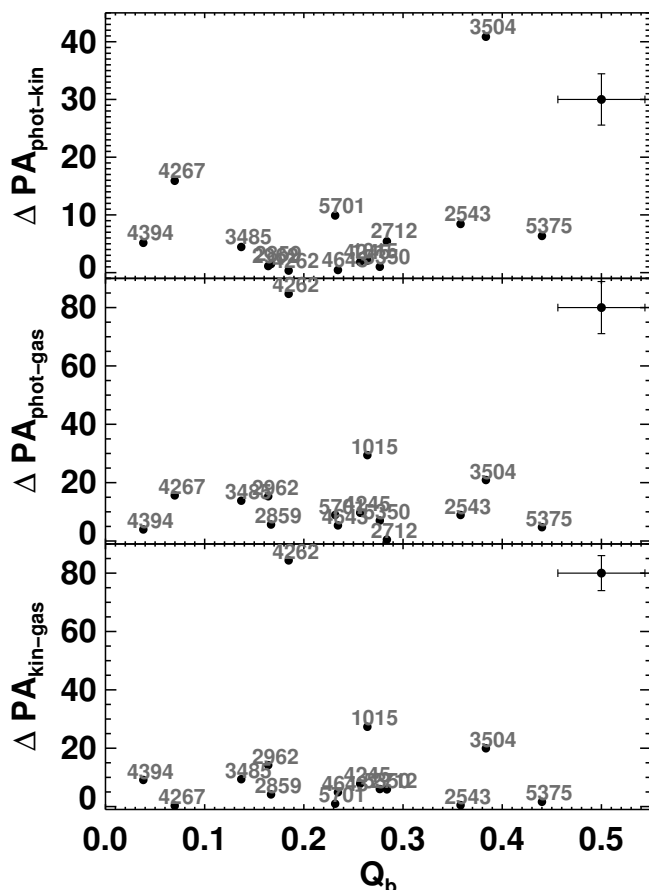


Figure 16. Photometric and kinematic position angle differences between stars and ionised gas as a function of bar strength. *Top*: difference between global photometric and stellar kinematic PA. *Middle*: difference of photometric to kinematic gas PA. *Bottom*: difference between the stellar kinematic and gas kinematic PA. Representative error bars are indicated in the top right corners.

No trends are observed with bar strength in any of the three cases. In previous studies including barred galaxies (e.g., Falcón-Barroso et al. 2006; Fathi et al. 2009; Krajnović et al. 2011; Barrera-Ballesteros et al. 2014), the observed misalignments were neither strong nor systematic. Misalignments were found mainly in systems with complex kinematics (non-regular rotators), systems in interaction and only in some barred galaxies, but their amplitudes largely depended on the FoV. The detailed study by Barrera-Ballesteros et al. (2014) further concludes that morphological substructures only influence the redistribution of angular momentum, but the global kinematics such as rotation are driven by the overall disc mass. Here, we also only detected one galaxy, NGC 3504, with a larger difference between the photometric and kinematic PAs. The ionised gas is known to react strongly to the bar producing a twist in the zero-velocity curve (e.g., Peterson & Huntley 1980; Emself et al. 2006). However, for the gas too, we only detected large misalignments in NGC 4262. The overall misalignment is slightly larger than that for the stellar kinematic/photometric PA difference, but not significantly. Finally, the difference between the two kinematic PAs (stellar and ionised gas PA) is found to be equally small and not correlated with the bar strength, confirming the results from earlier studies (as described above).

6.3 Stellar kinematic features related to bar strengths

Bars can be depicted as engines that, on the one hand, drive gas towards the central regions and consequently nourish star formation (e.g. Elmegreen & Elmegreen 1985, 1989; Erwin 2005; Ellison et al. 2011) and, on the other hand, support radial motions of stars (e.g., Minchev & Famaey 2010; Brunetti, Chiappini & Pfenniger 2011). Due to these factors, they are natural triggers of changes in the centre of galaxies, and in the stellar velocity dispersion in particular. We do not find, however, any trend between the central velocity dispersion and the bar strength. This reinforces the picture that the central stellar velocity dispersion is determined by global galaxy properties. At least, it does not vary significantly due to morphological substructures in a systematic way, except for the occasional central σ -drop.

While simulations predict and find a significant influence of the bar on the host galaxy in various ways (e.g., Martínez-Valpuesta, Shlosman & Heller 2006; Athanassoula, Machado & Rodionov 2013; Sellwood 2014), we only find mild signatures on the kinematic maps in our sample, such as the proposed double-hump rotation curve and occasional σ -drops. Despite this lack of major, bar-induced alterations in global galaxy kinematic parameters, we detect some relation between those subtle kinematic features and the bar strength. It is thus logical to assume a connection between those features and the bars.

Since double-humps and σ -drops exist commonly among barred galaxies, we tested their amplitude in relation to the bar strength. In other words, would stronger bars produce stronger humps or deeper drops? We quantified the strength of the hump by the difference of its inner peak and consecutive drop, calling this parameter ΔV . We further normalised this value by the maximum rotation – corrected for inclination – that we could detect for each galaxy. We are aware that asymmetric drift could attenuate this signal slightly, but do not expect a major change for the trend observed.

For the velocity dispersion we determined the amplitude of the central σ -drop if present, again normalised by the maximum velocity dispersion (following Peletier et al. 2012). We chose to compute these quantities at the position angle where the signal was stronger. Since the hump in the velocity is seen strongest along the major axis, we took the profile along that axis. We chose to take the velocity dispersion profiles along the bar major axis, because the drop is most pronounced along that direction.

Figure 17 shows the results. We identified galaxies with very low inclinations in light grey, galaxies with intermediate but still low inclinations or larger uncertainties in their velocity fields in grey, and reliable points in black. As our sample is very small, we did not discard any points, but indicate that we are conscious about the bias introduced by measuring at different inclinations. As inclination effects in the velocity dispersion are very difficult to characterise (i.e., it depends on the projection of the velocity ellipsoid being probed and anisotropy), we did not attempt any correction.

We find tentative evidence that stronger bars produce stronger humps in the velocity profile. After the inclination correction, the low-inclination galaxies also follow this trend and we obtain a linear Pearson correlation coefficient of $R=0.57$. Discarding unreliable galaxies (light gray points), the correlation coefficient increases to $R=0.76$. As the hump could sometimes be distinguished better in the ionised gas, we also determined these parameter in the gas velocity profile (not shown here). The results follow the same trend. In the bottom row of Fig. 17, we show the measurement of the magnitude of the σ -drop. Stronger bars produce a stronger σ -drop features. We obtained an overall linear Pearson correlation coeffi-

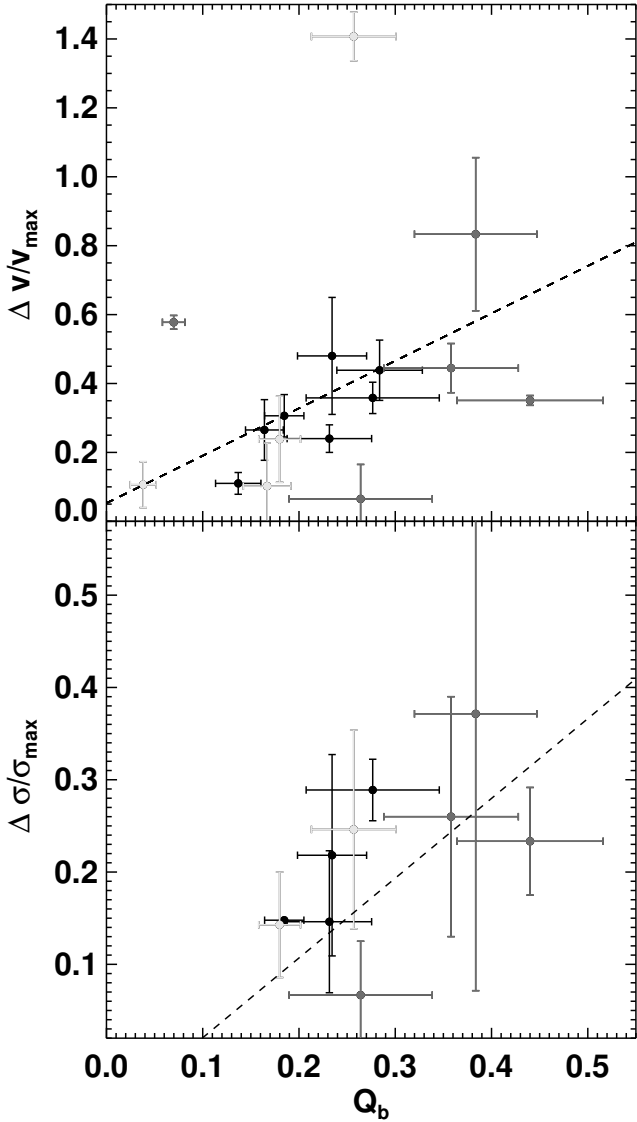


Figure 17. Different parameters detected in the kinematic maps of barred galaxies as a function of bar strength. *Top:* Magnitude of the velocity hump along the major axis rotation curve, normalised by the maximum rotation velocity and corrected for inclination (see text for details). *Bottom:* Magnitude of the σ -drop, normalised by the maximum dispersion (i.e. difference between central drop and highest surrounding velocity dispersion). In both panels, the dashed line indicates a linear fit to the black and dark gray points.

cient of $R=0.74$. All except one of the galaxies without a central dispersion drop have Q_b values below 0.15. The lack of this drop feature seems to be most evident in galaxies with weaker bars.

6.4 Stellar angular momentum as a function of bar strength

We now inspect the influence of the bar on the integrated angular momentum within one effective radii (λ_{Re}). This is shown in Fig. 18. The values obtained for λ_{Re} are consistent with the values found in the literature for barred galaxies (e.g. Bender, Saglia & Gerhard 1994; Krajnović et al. 2008, 2011). These studies, however, do not include bar strength measurements. We observe an increasing value of λ_{Re} with bar strength. This is somewhat connected to Hubble type, because the later-types in our sample display the

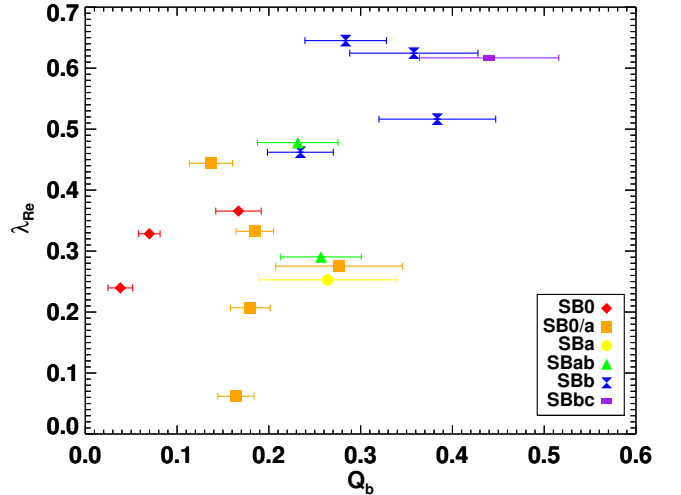


Figure 18. Apparent stellar angular momentum within one effective radius (Emsellem et al. 2007) as a function of bar strength. The different Hubble types are shown in different colours.

largest λ_{Re} values. The high λ_{Re} values observed in the later-type galaxies are likely due to the higher fraction of the disc, and thus high rotation, included within the one effective radius aperture.

As there is angular momentum transfer between the bar, disc and outer halo (e.g., Combes & Elmegreen 1993; Martínez-Valpuesta, Shlosman & Heller 2006), the value of λ_{Re} should be higher in barred galaxies compared to their non-barred counterparts. Athanassoula (2003) showed, however, that while angular momentum is transferred to the disc, the bar also slows down and therefore contributes to a decrease in λ_{Re} . The current available λ_{Re} values in the ATLAS3D (Emsellem et al. 2011) or CALIFA samples (Falcón-Barroso et al. 2014) do not indicate distinct values for barred and non-barred galaxies.

6.5 Bars as drivers of radial motions

Bars have been studied as a major driver of radial mixing for a long time (e.g. Friedli & Benz 1993), but spiral arms (e.g., Sellwood & Binney 2002) or the combination of their resonance overlap (e.g., Minchev & Famaey 2010; Shevchenko 2011) are also held responsible for an increase of this. Investigating the latter, Brunetti, Chiappini & Pfenniger (2011) found that kinematically hot discs are not as efficient environments and exhibit less radial mixing than kinematically colder ones. We investigate the level of radial motions induced by bars in our sample by studying the radial gradients of the stellar velocity dispersion. The expectation is that barred galaxies would display flatter gradients than those measured in non-barred systems.

We start by comparing velocity dispersion profiles along the major and minor axes of the bar. In earlier literature studies, velocity dispersion profiles were investigated typically only along the major axis of the bar (e.g. Pérez, Sánchez-Blázquez & Zurita 2009). For our sample, this is shown in Fig. 19 for one galaxy as an example (similar plots for other galaxies are presented in Appendix C). We show the overall stellar velocity dispersion map for reference and, next to it, the radial profiles along the major and minor axes (minor axis radii are corrected for inclination) of the bar extracted from this map. The profiles along the axes are generally overlapping, hence we do not observe any increase along the bar major axis. In one third of our sample, however, we observe a mild dif-

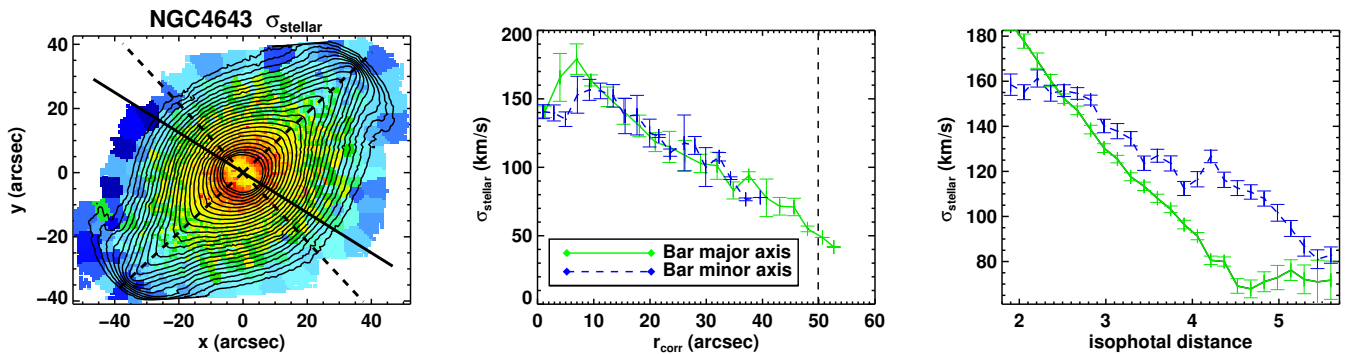


Figure 19. Stellar velocity dispersion map of NGC 4643 and associated profiles. (*Left*) Stellar velocity dispersion map with bar major and minor axes indicated with dashed lines. (*Middle*) Averaged profiles, corrected for inclination. Dashed line indicates the bar length. (*Right*) Averaged profiles along isophotes (first point corresponds to first isophote seen on the top left image).

ference around the central parts (also seen in the example), with the major axis showing a higher dispersion. This is probably linked to the aforementioned kinematic substructures such as inner discs or rings, possibly a result of barred secular evolution. The major axis profiles observed in Pérez, Sánchez-Blázquez & Zurita (2009) show a similar behavior to ours, but no minor axis measurements have been performed in that work.

As bars are structures seen in the photometry, we decided to also trace the profile comparing their points along the same isophotes. The isophotal profiles reveal a larger overall σ along of the major axis than the minor axis, and not just in the central parts. The fact that the velocity dispersion further out is higher along the minor axis, compared with the same isophote on the major axis, shows that the dispersion of the bulge – traced by the minor axis – dominates strongly, regardless of the prominent bar seen in the photometry. It shows nonetheless that the kinematics of the bar is significantly different than the bulge and it is more similar to the disc, because at the outer end of the profiles, reaching the disc, values along the major and minor axes start coinciding again.

Figure 20 shows a relation between the outer gradient of the stellar velocity dispersion and the bar strength. The gradient is shallower for stronger bars. Nevertheless, the trend is based on only very few points, in particular in the low bar strength regime. The presence of a bar can cause enhanced radial motions which perturb the system. Thus the orbital mixing increases which in turn can lead to higher dispersion and shallower gradients. This could be the reason for the observed flattening of the gradients with higher Q_b . Additionally, we measured the gradient not only along the major axis of the galaxy (black points), but also along the minor axis (blue points). If the bar would significantly flatten the gradient along the major axis, the minor axis values would be expected to show steeper gradients. The results, however, show a scatter of shallower as well as steeper gradients along the minor axes compared to the points measured along the major axes and we cannot identify a systematic behavior.

The measurement of the maximal radial velocities that we use to calculate the kinematic torques also indicate the average radial displacement. As mentioned in previous sections, the average radial motion is much higher in the gas than for the stars. Stars move at velocities between 10 and 60 km/s radially, corresponding to about 10-60 kpc/Gyr or 0.09 - 0.88 when normalised with the rotation at $\approx r_e$, a value which is similar in magnitudes to what we find with our own simulations (e.g. in I_4 it is around 0.2) whereas the gas move at 40 - 100 km/s and in extreme cases such as NGC 4262 at more than 300 km/s. The latter is most probably due to an outer

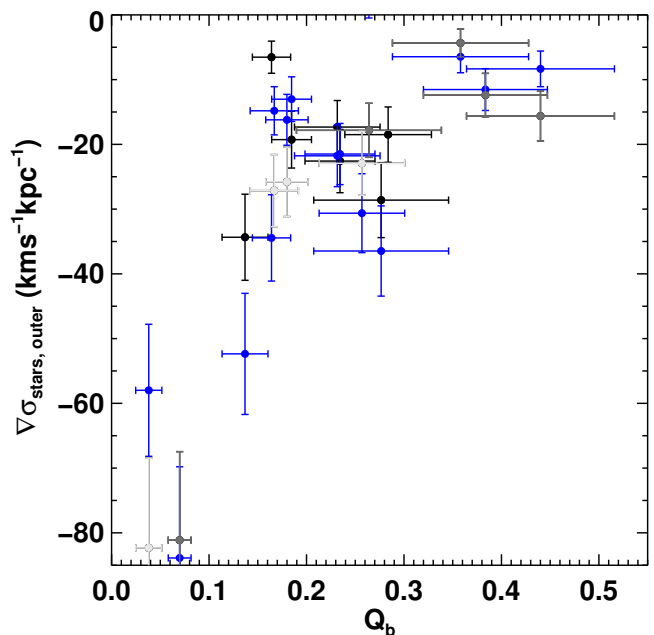


Figure 20. Gradient of the outer velocity dispersion, ignoring the central regions, as a function of bar strength. Blue points indicate profiles taken along the bar minor axis, while black points show the ones along the bar major axis.

influence such as an interaction (Vollmer, Huchtmeier & van Driel 2005). Nevertheless, the stronger effect on the gas than on the stars has been seen in numerous simulations (Athanasoula, Machado & Rodionov 2013; Kubryk, Prantzos & Athanasoula 2013, e.g.). Kubryk, Prantzos & Athanasoula (2014) find a particular influence of the bar-induced radial inflow on the gaseous profile. Furthermore, Maciejewski, Emsellem & Krajnović (2012) obtain values which are in the range of the ones we recover using the same method. The recent work of Goz et al. (2015) analyzing two simulations of barred galaxies resulting from N-body+SPH cosmological simulations, shows one case with significantly higher radial motions (around 150 km/s) whereas in the other case the magnitude is comparable to what we observe (around 30 km/s).

In a large number of simulations (e.g., Minchev et al. 2012) bars are found to be the most efficient driver of radial migration, in particular through their corotation resonance. We have not yet determined the radius of corotation for our sample, but plan to com-

pute this in a forthcoming paper. This parameter, together with the stellar populations will further complete the picture of bar-induced mixing. In particular in Paper II of this series, we will assess the impact of the radial motions determined here, on the stellar population properties, which will allow us to shed light onto radial migration effects (e.g., Friedli, Benz & Kennicutt 1994; Haywood 2008; Roediger et al. 2012; Kubryk, Prantzos & Athanassoula 2013).

7 SUMMARY AND CONCLUSIONS

We present the BaLROG sample of 16 barred galaxies of different Hubble types, spanning the typical bar strengths found in the local Universe. Our large mosaics with the integral field unit SAURON cover the bars out to the radius where the disc begins to dominate, at a spatial resolution of typically 100 pc. For every galaxy we also use *Spitzer* observations from the S⁴G survey of nearby galaxies (Sheth et al. 2010) to determine several photometric parameters, as well as to derive the bar strength Q_b . From the velocity maps, we calculate radial and tangential velocities to compute the bar strength based on the kinematics, Q_{kin} . Our aim is to establish a reliable yardstick, namely bar strength, to probe the influence of the bars on different parameters of the host galaxies.

In this paper we focus on the kinematics of the galaxies, deriving stellar and gas velocities and velocity dispersions, h_3 and h_4 Gauss-Hermite moments and the stellar angular momentum λ_R and carefully comparing to a large set of N-body simulations. The analysis of our observations leads to the following results and conclusions:

- Bars do not strongly influence the global kinematics of their host galaxies, regardless of their strength. Our work confirms previous studies (e.g. Falcón-Barroso et al. 2006; Fathi et al. 2009; Krajnović et al. 2011; Barrera-Ballesteros et al. 2014) and shows the lack of strong kinematic misalignments between the galaxies' photometric and kinematic axes.

- Bars do have an influence on more subtle kinematic features, especially in the inner regions of galaxies. We detect double-hump velocity profiles and velocity dispersion drops (e.g., Bureau & Athanassoula 2005), which increase in intensity with increasing bar strength.

- We find evidence for the presence of inner structures such as inner rings or discs in about 50% of our sample. These features are detected from the anti-correlation between h_3 and V/σ within the effective radius of the galaxies (≈ 0.1 bar lengths).

- The derived λ_R profiles show a dip at $0.2 \pm 0.1 R_{bar}$, which we suggest is connected to the presence of inner substructures.

- We also derived the integrated angular momentum within one effective radius (λ_{Re}) and find that galaxies with stronger bars exhibit a higher λ_{Re} value. This may be a secondary effect of late-type galaxies, because they are more rotationally supported and thus also host stronger bars.

- We developed a new method to determine the bar strength from stellar or ionised gas velocity maps (Q_{kin}). This method relies on the extraction of the ratio of radial and tangential velocities using the technique developed by Maciejewski, Emsellem & Krajnović (2012). Values of this parameter agree well with independent measurements obtained from imaging, Q_b , e.g., Laurikainen & Salo (2002), and predictions from numerical N-body simulations.

- Bar strength values measured from ionised-gas kinematic maps are a factor ~ 2.5 larger than those determined from the stellar kinematic maps.

- We observe a flattening of the outer stellar velocity dispersion profiles with increasing bar strength.

These results suggest a complex influence of bars in nearby galaxies, especially affecting central regions. We do not observe a significant influence on global properties, but bars seem to affect only on small scales. The gas is clearly more strongly affected, reflected in higher gaseous than stellar torques. In our sample we detect a difference between bars in early and late-type galaxies hinting towards a different mechanism, maybe due to the presence of higher and lower gas fractions. To better answer these questions and determine time scales, we will investigate the stellar populations of these galaxies in detail in BaLROG II (Seidel et al., in prep) and also determine their corotation radii and pattern speeds in relation with their dark matter fractions (BaLROG III).

ACKNOWLEDGMENTS

We would like to thank Alfonso Aguerri for stimulating comments and discussion and Martin Stringer for editorial help. MKS and JFB wish to express their gratitude to the Roque de los Muchachos Observatory on La Palma and the different operators of the William Herschel Telescope during our numerous runs, as well as observing support by Agnieszka Rys, Carolin Wittman and Thorsten Lisker. We also acknowledge support from grant AYA2013-48226-C3-1-P from the Spanish Ministry of Economy and Competitiveness (MINECO). IMV acknowledges support from grant AYA2009-11137. JHK acknowledges the support from grant AYA2013-41243-P. MKS acknowledges the support of the Instituto de Astrofísica de Canarias via an Astrophysicist Resident fellowship. We also acknowledge support from the FP7 Marie Curie Actions of the European Commission, via the Initial Training Network DAGAL under REA grant agreement number 289313. This research made use of Montage, funded by the National Aeronautics and Space Administration's Earth Science Technology Office, Computational Technologies Project, under Cooperative Agreement Number NCC5-626 between NASA and the California Institute of Technology. The code is maintained by the NASA/IPAC Infrared Science Archive. This research has made use of the NASA/IPAC Extragalactic Database (NED) which is operated by the Jet Propulsion Laboratory, California Institute of Technology, under contract with the National Aeronautics and Space Administration. The paper is based on observations obtained at the William Herschel Telescope, operated by the Isaac Newton Group in the Spanish Observatorio del Roque de los Muchachos of the Instituto de Astrofísica de Canarias.

REFERENCES

- Abraham R. G., van den Bergh S., Glazebrook K., Ellis R. S., Santiago B. X., Surma P., Griffiths R. E., 1996, *ApJS*, 107, 1
Aguerri J. A. L., Beckman J. E., Prieto M., 1998, *AJ*, 116, 2136
Aguerri J. A. L., Méndez-Abreu J., Corsini E. M., 2009, *A&A*, 495, 491
Athanassoula E., 1992a, *MNRAS*, 259, 328
Athanassoula E., 1992b, *MNRAS*, 259, 345
Athanassoula E., 2003, *MNRAS*, 341, 1179
Athanassoula E., 2005, *MNRAS*, 358, 1477
Athanassoula E., Machado R. E. G., Rodionov S. A., 2013, *MNRAS*, 429, 1949
Bacon R. et al., 2001, *MNRAS*, 326, 23

- Barazza F. D., Jogee S., Marinova I., 2008, *ApJ*, 675, 1194
- Barrera-Ballesteros J. K. et al., 2014, *A&A*, 568, A70
- Bender R., Saglia R. P., Gerhard O. E., 1994, *MNRAS*, 269, 785
- Blitz L., Spergel D. N., 1991, *ApJ*, 379, 631
- Block D. L., Buta R., Knapen J. H., Elmegreen D. M., Elmegreen B. G., Puerari I., 2004, *AJ*, 128, 183
- Bournaud F., Combes F., Semelin B., 2005, *MNRAS*, 364, L18
- Brunetti M., Chiappini C., Pfenniger D., 2011, *A&A*, 534, A75
- Bureau M., Athanassoula E., 2005, *ApJ*, 626, 159
- Bureau M., Athanassoula E., Chung A., Aronica G., 2004, in *Astrophysics and Space Science Library*, Vol. 319, *Penetrating Bars Through Masks of Cosmic Dust*, Block D. L., Puerari I., Freeman K. C., Gross R., Block E. K., eds., p. 139
- Bureau M., Freeman K. C., 1999, *AJ*, 118, 126
- Buta R., Block D. L., 2001, *ApJ*, 550, 243
- Buta R., Crocker D. A., 1993, *AJ*, 105, 1344
- Buta R., Laurikainen E., Salo H., Knapen J. H., 2010, *ApJ*, 721, 259
- Buta R. et al., 2015, *ArXiv e-prints*
- Buta R., van Driel W., Braine J., Combes F., Wakamatsu K., Sofue Y., Tomita A., 1995, *ApJ*, 450, 593
- Buta R., Vasylyev S., Salo H., Laurikainen E., 2005, *AJ*, 130, 506
- Byrd G., Rautiainen P., Salo H., Buta R., Crocher D. A., 1994, *AJ*, 108, 476
- Cappellari M., Copin Y., 2003, *MNRAS*, 342, 345
- Cappellari M., Emsellem E., 2004, *The Publications of the Astronomical Society of the Pacific*, 116, 138
- Chung A., Bureau M., 2004, *AJ*, 127, 3192
- Cisternas M., Sheth K., Salvato M., Knapen J. H., Civano F., Santini P., 2014, *ArXiv e-prints*
- Coelho P., Gadotti D. A., 2011, *ApJ*, 743, L13
- Combes F., Elmegreen B. G., 1993, *A&A*, 271, 391
- Combes F., Sanders R. H., 1981, *A&A*, 96, 164
- Comerón S., Knapen J. H., Beckman J. E., Laurikainen E., Salo H., Martínez-Valpuesta I., Buta R. J., 2010, *MNRAS*, 402, 2462
- de Grijs R., 1998, *MNRAS*, 299, 595
- de Vaucouleurs G., de Vaucouleurs A., Corwin, Jr. H. G., Buta R. J., Paturel G., Fouqué P., 1991, *Third Reference Catalogue of Bright Galaxies. Volume I: Explanations and references. Volume II: Data for galaxies between 0^h and 12^h . Volume III: Data for galaxies between 12^h and 24^h .*
- Debattista V. P., Carollo C. M., Mayer L., Moore B., 2005, *ApJ*, 628, 678
- Debattista V. P., Sellwood J. A., 2000, *ApJ*, 543, 704
- Ellison S. L., Nair P., Patton D. R., Scudder J. M., Mendel J. T., Simard L., 2011, *MNRAS*, 416, 2182
- Elmegreen B. G., 1994, *ApJ*, 425, L73
- Elmegreen B. G., Elmegreen D. M., 1985, *ApJ*, 288, 438
- Elmegreen B. G., Elmegreen D. M., 1989, *ApJ*, 342, 677
- Elmegreen B. G., Elmegreen D. M., Hirst A. C., 2004, *ApJ*, 612, 191
- Elmegreen D. M., Chromey F. R., Santos M., Marshall D., 1997, *AJ*, 114, 1850
- Emsellem E. et al., 2011, *MNRAS*, 414, 888
- Emsellem E. et al., 2007, *MNRAS*, 379, 401
- Emsellem E., Fathi K., Wozniak H., Ferruit P., Mundell C. G., Schinnerer E., 2006, *MNRAS*, 365, 367
- Erwin P., 2004, *A&A*, 415, 941
- Erwin P., 2005, *MNRAS*, 364, 283
- Erwin P., Sparke L. S., 2002, *AJ*, 124, 65
- Eskridge P. B. et al., 2000, *AJ*, 119, 536
- Falcón-Barroso J. et al., 2006, *MNRAS*, 369, 529
- Falcón-Barroso J., Lyubenova M., van de Ven G., the CALIFA collaboration, 2014, *ArXiv e-prints*
- Falcón-Barroso J., Sánchez-Blázquez P., Vazdekis A., Ricciardelli E., Cardiel N., Cenarro A. J., Gorgas J., Peletier R. F., 2011, *Astronomy and Astrophysics*, 532, A95
- Fathi K., Beckman J. E., Piñol-Ferrer N., Hernandez O., Martínez-Valpuesta I., Carignan C., 2009, *ApJ*, 704, 1657
- Fathi K., Peletier R. F., 2003, *A&A*, 407, 61
- Friedli D., Benz W., 1993, *A&A*, 268, 65
- Friedli D., Benz W., Kennicutt R., 1994, *ApJ*, 430, L105
- Fukuda H., Habe A., Wada K., 2000, *ApJ*, 529, 109
- Gadotti D. A., de Souza R. E., 2006, *ApJS*, 163, 270
- Gadotti D. A., dos Anjos S., 2001, *AJ*, 122, 1298
- Gerhard O. E., 1993, *MNRAS*, 265, 213
- Goz D., Monaco P., Murante G., Curir A., 2015, *MNRAS*, 447, 1774
- Haywood M., 2008, *MNRAS*, 388, 1175
- Howard C. D. et al., 2009, *ApJ*, 702, L153
- Hubble E. P., 1936, *Realm of the Nebulae*. Yale University Press
- Jogee S. et al., 2004, *ApJ*, 615, L105
- Kim T. et al., 2014, *ApJ*, 782, 64
- Kim W.-T., Seo W.-Y., Stone J. M., Yoon D., Teuben P. J., 2012, *ApJ*, 747, 60
- Kim W.-T., Stone J. M., 2012, *ApJ*, 751, 124
- Knapen J. H., Beckman J. E., Heller C. H., Shlosman I., de Jong R. S., 1995, *ApJ*, 454, 623
- Knapen J. H., Shlosman I., Peletier R. F., 2000, *ApJ*, 529, 93
- Kormendy J., Kennicutt, Jr. R. C., 2004, *Annual Review of Astronomy & Astrophysics*, 42, 603
- Krajnović D. et al., 2008, *MNRAS*, 390, 93
- Krajnović D. et al., 2011, *MNRAS*, 414, 2923
- Kroupa P., 2001, *MNRAS*, 322, 231
- Kubryk M., Prantzos N., Athanassoula E., 2013, *MNRAS*, 436, 1479
- Kubryk M., Prantzos N., Athanassoula E., 2014, *ArXiv e-prints*
- Laurikainen E., Salo H., 2002, *MNRAS*, 337, 1118
- Laurikainen E., Salo H., Buta R., Knapen J. H., 2007, *MNRAS*, 381, 401
- Laurikainen E., Salo H., Buta R., Knapen J. H., 2011, *MNRAS*, 418, 1452
- Laurikainen E., Salo H., Buta R., Vasylyev S., 2004, *MNRAS*, 355, 1251
- Łokas E. L., Athanassoula E., Debattista V. P., Valluri M., Pino A. d., Senczuk M., Gajda G., Kowalczyk K., 2014, *MNRAS*, 445, 1339
- Maciejewski W., Emsellem E., Krajnović D., 2012, *MNRAS*, 427, 3427
- Marinova I., Jogee S., 2007, *ApJ*, 659, 1176
- Martin P., 1995, *AJ*, 109, 2428
- Martin P., Roy J.-R., 1994, *ApJ*, 424, 599
- Martinet L., Friedli D., 1997, *A&A*, 323, 363
- Martínez-Valpuesta I., Gerhard O., 2011, *ApJ*, 734, L20
- Martínez-Valpuesta I., Shlosman I., Heller C., 2006, *ApJ*, 637, 214
- Masters K. L. et al., 2011, *MNRAS*, 411, 2026
- Méndez-Abreu J., Corsini E. M., Debattista V. P., De Rijcke S., Aguerri J. A. L., Pizzella A., 2008, *ApJ*, 679, L73
- Méndez-Abreu J., Debattista V. P., Corsini E. M., Aguerri J. A. L., 2014, *A&A*, 572, A25
- Méndez-Abreu J., Sánchez-Janssen R., Aguerri J. A. L., 2010, *ApJ*, 711, L61
- Menéndez-Delmestre K., Sheth K., Schinnerer E., Jarrett T. H., Scoville N. Z., 2007, *ApJ*, 657, 790

- Mínchev I., Famaey B., 2010, *ApJ*, 722, 112
- Mínchev I., Famaey B., Quillen A. C., Di Matteo P., Combes F., Vlajić M., Erwin P., Bland-Hawthorn J., 2012, *A&A*, 548, A126
- Nair P. B., Abraham R. G., 2010, *ApJ*, 714, L260
- Ness M. et al., 2013, *MNRAS*, 432, 2092
- Peeples M. S., Martini P., 2006, *ApJ*, 652, 1097
- Peletier R. F. et al., 2012, *MNRAS*, 419, 2031
- Pérez I., Aguerri J. A. L., Méndez-Abreu J., 2012, *A&A*, 540, A103
- Pérez I., Sánchez-Blázquez P., 2011, *A&A*, 529, A64
- Pérez I., Sánchez-Blázquez P., Zurita A., 2009, *A&A*, 495, 775
- Peterson C. J., Huntley J. M., 1980, *ApJ*, 242, 913
- Pfenniger D., Norman C., 1990, *ApJ*, 363, 391
- Piñol-Ferrer N., Fathi K., Carignan C., Font J., Hernandez O., Karlsson R., van de Ven G., 2014, *MNRAS*, 438, 971
- Planck Collaboration et al., 2014, *A&A*, 571, A16
- Regan M. W., Teuben P., 2003, *ApJ*, 582, 723
- Roediger J. C., Courteau S., Sánchez-Blázquez P., McDonald M., 2012, *ApJ*, 758, 41
- Sakamoto K., Okumura S. K., Ishizuki S., Scoville N. Z., 1999, *ApJ*, 525, 691
- Salo H., Laurikainen E., Buta R., Knapen J. H., 2010, *ApJ*, 715, L56
- Salo H., Rautiainen P., Buta R., Purcell G. B., Cobb M. L., Crocker D. A., Laurikainen E., 1999, *AJ*, 117, 792
- Sánchez-Blázquez P., Ocvirk P., Gibson B. K., Pérez I., Peletier R. F., 2011, *MNRAS*, 415, 709
- Sánchez-Blázquez P. et al., 2006, *MNRAS*, 371, 703
- Sánchez-Blázquez P. et al., 2014, *A&A*, 570, A6
- Sarzi M. et al., 2006, *MNRAS*, 366, 1151
- Schwarz M. P., 1981, *ApJ*, 247, 77
- Sellwood J. A., 2014, *Reviews of Modern Physics*, 86, 1
- Sellwood J. A., Binney J. J., 2002, *MNRAS*, 336, 785
- Shen J., Sellwood J. A., 2004, *ApJ*, 604, 614
- Sheth K. et al., 2008, *ApJ*, 675, 1141
- Sheth K. et al., 2010, *PASP*, 122, 1397
- Sheth K., Vogel S. N., Regan M. W., Thornley M. D., Teuben P. J., 2005, *ApJ*, 632, 217
- Shevchenko I. I., 2011, *ApJ*, 733, 39
- Simmons B. D. et al., 2014, *MNRAS*, 445, 3466
- Skrutskie M. F. et al., 2006, *AJ*, 131, 1163
- Speltinck T., Laurikainen E., Salo H., 2008, *MNRAS*, 383, 317
- van de Ven G., Chang P., 2009, *ApJ*, 697, 619
- van der Marel R. P., Franx M., 1993, *ApJ*, 407, 525
- Vazdekis A., Sánchez-Blázquez P., Falcón-Barroso J., Cenarro A. J., Beasley M. A., Cardiel N., Gorgas J., Peletier R. F., 2010, *MNRAS*, 404, 1639
- Vollmer B., Huchtmeier W., van Driel W., 2005, *A&A*, 439, 921
- Wang Y., Zhao H., Mao S., Rich R. M., 2012, *MNRAS*, 427, 1429
- Whyte L. F., Abraham R. G., Merrifield M. R., Eskridge P. B., Frogel J. A., Pogge R. W., 2002, *MNRAS*, 336, 1281
- Wozniak H., Combes F., Emsellem E., Friedli D., 2003, *A&A*, 409, 469

APPENDIX A: DESCRIPTION OF THE SIMULATIONS

In the following we illustrate the give a more detailed description of the simulations and how we used to obtain the torque measures. Figure A1 shows as an example the intensity and velocity maps of one of the snapshots of the I_3 simulation at an intermediate time step, at an inclination of 30 degree and a bar-to-line-of-nodes-PA of 55 degree. Figure A2 shows the corresponding obtained radial and tangential velocities. In Fig. A3, the full time series (all 1800 snapshots) of this particular simulation is shown. The early very strong peak is associated with the first buckling of this bar (not stable in time). The shape of the obtained curve indicating the kinematical torque values resembles the curve of the A2 value measured during the simulation and also gives an indication on the bar strength. For the other simulations series, these measurements along with the shape of the final curve differs significantly.

The variations of Q_{kin} with inclination and PA (shown with different colors and symbols respectively in Fig. A3 are due to the fact that the assumptions of a thin disc and stable bar are not 100% correct. This is the case especially during the buckling event of the bar and during the later stages of the evolution, which is to be expected due to the thickening of the bar. If it was a perfect measurement, all points should overlap vertically, since we simply rotate the simulated galaxy slightly in order to achieve its different orientation. Since the buckling event is a short moment during bar evolution, we can safely exclude these points from our comparison as the likelihood to find a bar in the buckling phase is rather low. Without these points and below $t=200$, the measurements agree rather well. A more extensive test can also be found in the Appendix B.

To perform the analysis for the comparison of the two torque measurements, we calculated the values of Q_b (in addition to those of Q_{kin}) for all sets of simulations in the same way as done for the observations. In Fig. 12 we presented the final results showing the observational measurements overlaid on the four simulations, I_1 , I_2 , I_3 and I_4 (level of disc-to-total ratios: 0.92, 0.62, 0.43, 0.29 respectively).

As seen in Fig. 12, none of the simulation series coincides perfectly with all the data points, but instead form a continuum. It is reassuring however that the simulation series fall onto the same relation found as for the observations.

Simulation I_1 (92% disk, shown by the green points) best represents the lower bar strengths. With decreasing disc content, the both the photometric and kinematic bar strengths increase. We also distinguish a particular behavior for I_4 : compared to the other sets, this series seems to adapt to all ranges starting from very weak to very strong bars. This is the simulation with the lowest disc percentage within the bar region initially and also after halo relaxation and is at every point in time submaximal. Overall, we find a trend of stronger bar development with increasing dark matter halo fraction in our simulations.

Comparing the velocity maps of the three different simulations with the observations, we find good agreement, especially in the case of I_1 . Simulations I_3 and I_4 in particular develop strong distortions in the stellar velocity fields which are not as pronounced in our observations. However, the bar strength of I_1 never reaches a higher value than about 0.2-0.3, unlike the observations. To reach higher values, we needed to increase the halo fraction.

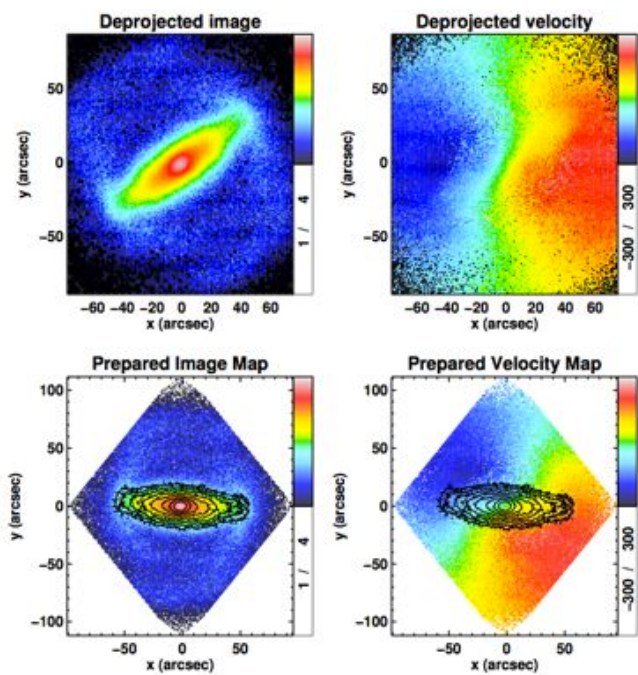


Figure A1. Intensity (in logarithmic units) and velocity maps (translated in km/s) of one of the snapshots of the I_3 simulation at an intermediate point of the bar evolution ($t=150$ at PA = 35 and inclination = 30). The bottom panels show the prepared maps which can be symmetrised by the code, with the bar in a horizontal position and adjusted field extensions. In those, we overlay the isophotes.

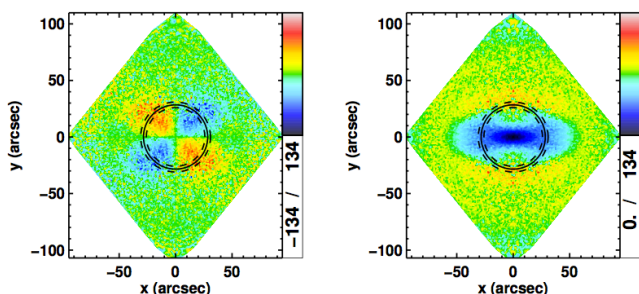


Figure A2. The obtained radial and tangential velocities for the simulated galaxy above, but now symmetrised.

APPENDIX B: INFLUENCE OF THE INCLINATION AND PA ON THE BAR STRENGTH MEASUREMENTS

We used four simulation sets (I_1 , I_2 , I_3 and I_4) to test the influence of PA and inclination on the bar strength measurements, namely Q_b , Q_{kin} and A2, on a large enough sample. Figure B1 illustrates those tests with the example of the I_2 simulation.

In the majority of cases the influence of these two parameters causes a consistent change in any of the different bar strength measurement methods. The PA influence always shows a clear trend: larger PAs result in higher strength values overall. Furthermore it causes less spread within the distinct inclinations, especially for Q_b and A2.

The effect of inclination is two-fold: in the simulations with higher disc-percentages (I_1 and I_2), its effect is reversed for low and high PAs. For low PAs, we detect that a lower inclination results in

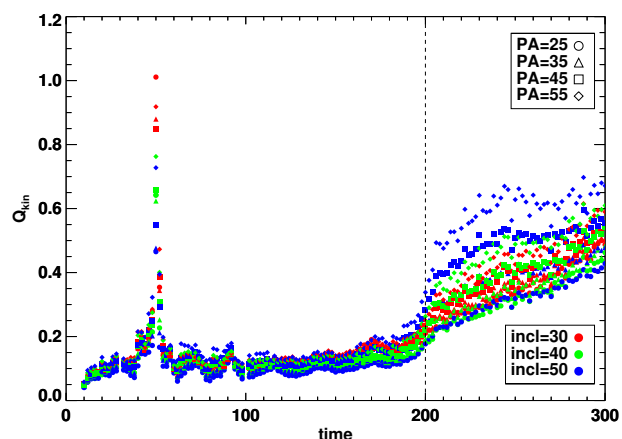


Figure A3. The kinematical torque evolution for one complete simulation, here I_3 as an example, indicating different inclinations and PAs. The dotted line indicates the point in time where the bar has reached its full strength and further evolution is not reliable, hence points to the right of it will not be considered in our analyses.

higher values in all three parameters, whereas for higher PAs, high inclinations result in higher values overall. The spread here is less.

For the other two simulations with higher DM content (I_3 and I_4), the effect of inclination is always the same despite the distinct PAs: a lower inclination results in higher values in the three measured parameters. Again, the spread is less at higher PAs (except for Q_{kin} in I_4).

The fact that the influences are similar in spite of the different measurement methods probably helps to produce the observed relation between them. It is important to bear the influence of these parameters in mind when checking the observations: low inclinations might lead to higher values, and, depending on the PA and DM fraction, high inclinations can also lead to lower values.

We also compared Q_b with the A2 values directly from the simulations and find that Q_b resembles A2 very well.

Overall, values of Q_b are expected to be higher at lower inclinations whereas values of Q_{kin} should be higher at higher inclinations as motions can be better measured with increased inclination. Our tests, however, suggest that in almost all cases, the chosen methods indicate a lower limit for the bar strength, in particular in the case of Q_b .

APPENDIX C: COMPLETE KINEMATIC MAPS FOR STARS AND IONISED GAS

We show maps of the stellar and ionised-gas kinematics for the entire BaLROG sample of galaxies in figures C1 to C16. In each figure we show different maps of each galaxy, top to bottom and left to right: first row: (i) S^4G image of the galaxy with an estimate of the final SAURON mosaic and the number of pointings indicated in the left lower corner, (ii) fundamental parameters of the galaxy along with the systemic velocity, inclination, stellar angular momentum within one effective radius and the bar strengths measured; second row: (i) surface brightness derived from the SAURON cube (collapsed in wavelength, shown in logarithmic scale), (ii) stellar mean velocity V (in km s^{-1}), (iii) stellar velocity dispersion σ (in km s^{-1}); third row: (i) flux of the ionised gas, based on [OIII] (shown

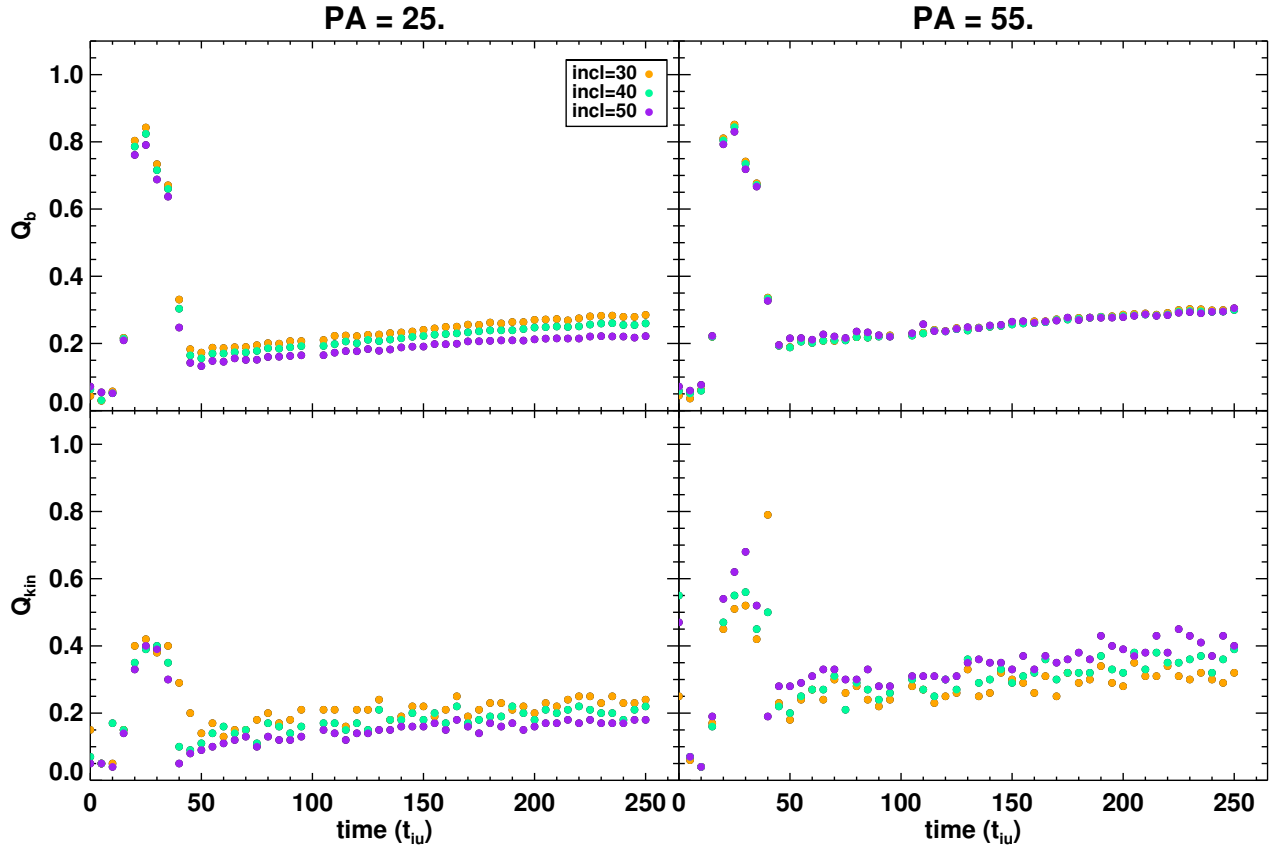
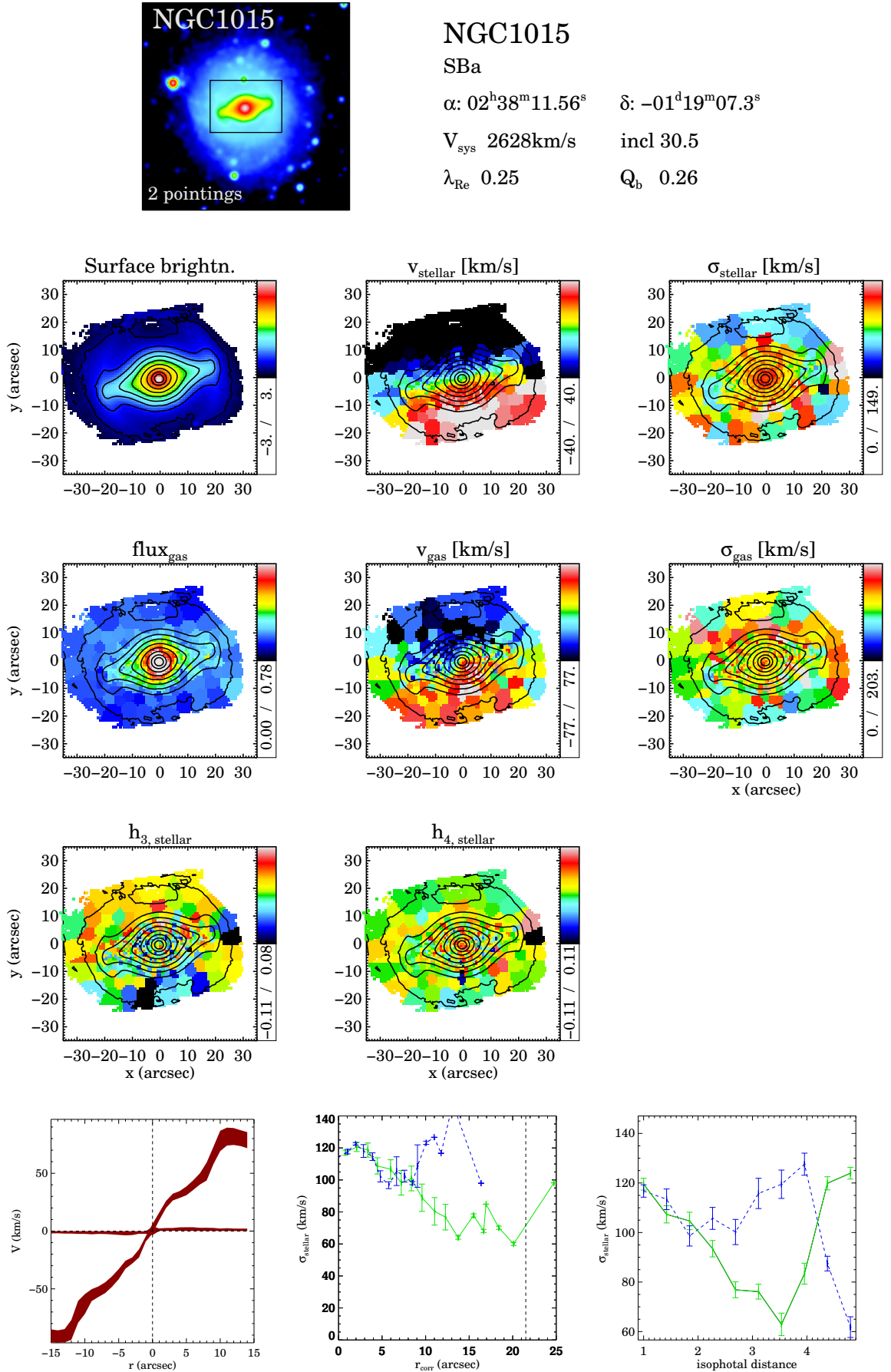


Figure B1. For a simulation with 60% disc we plot Q_b and Q_{kin} versus time for different inclinations and PAs: left: PA=25, right: PA=55. Top: Q_b and bottom: Q_{kin} . The elevation at early times is due to the buckling event in the bar evolution.

as square-root-scaled), (ii) mean radial ionised gas velocity, (iii) ionised gas velocity dispersion (in km s^{-1}); fourth row: (i) Gauss-Hermite moments h_3 and (ii) h_4 ; fifth row: (i) major and minor axis rotation curves of the stellar velocity, (ii) radial profile (inclination corrected) of the stellar velocity dispersion of the major and minor axis of the bar, (iii) isophotal profile of the stellar velocity dispersion along bar major and minor axis. The cut levels are indicated in a box on the right-hand side of each map.



© 2015 RAS, MNRAS 000, 1–22 **Figure C1.** Summary of the kinematic maps for stars and ionised gas for each galaxy.

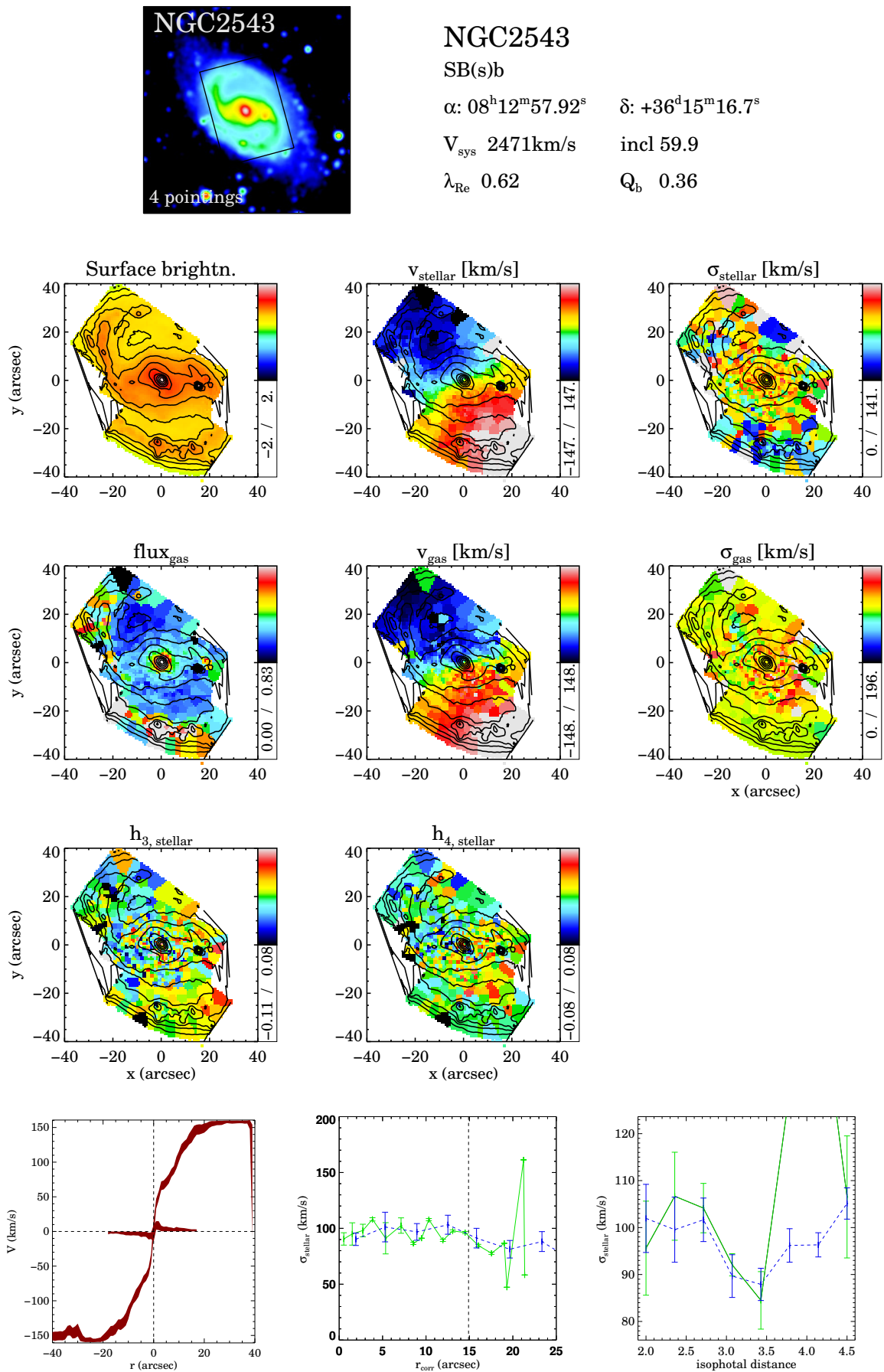


Figure C2. Figure C1 continued.

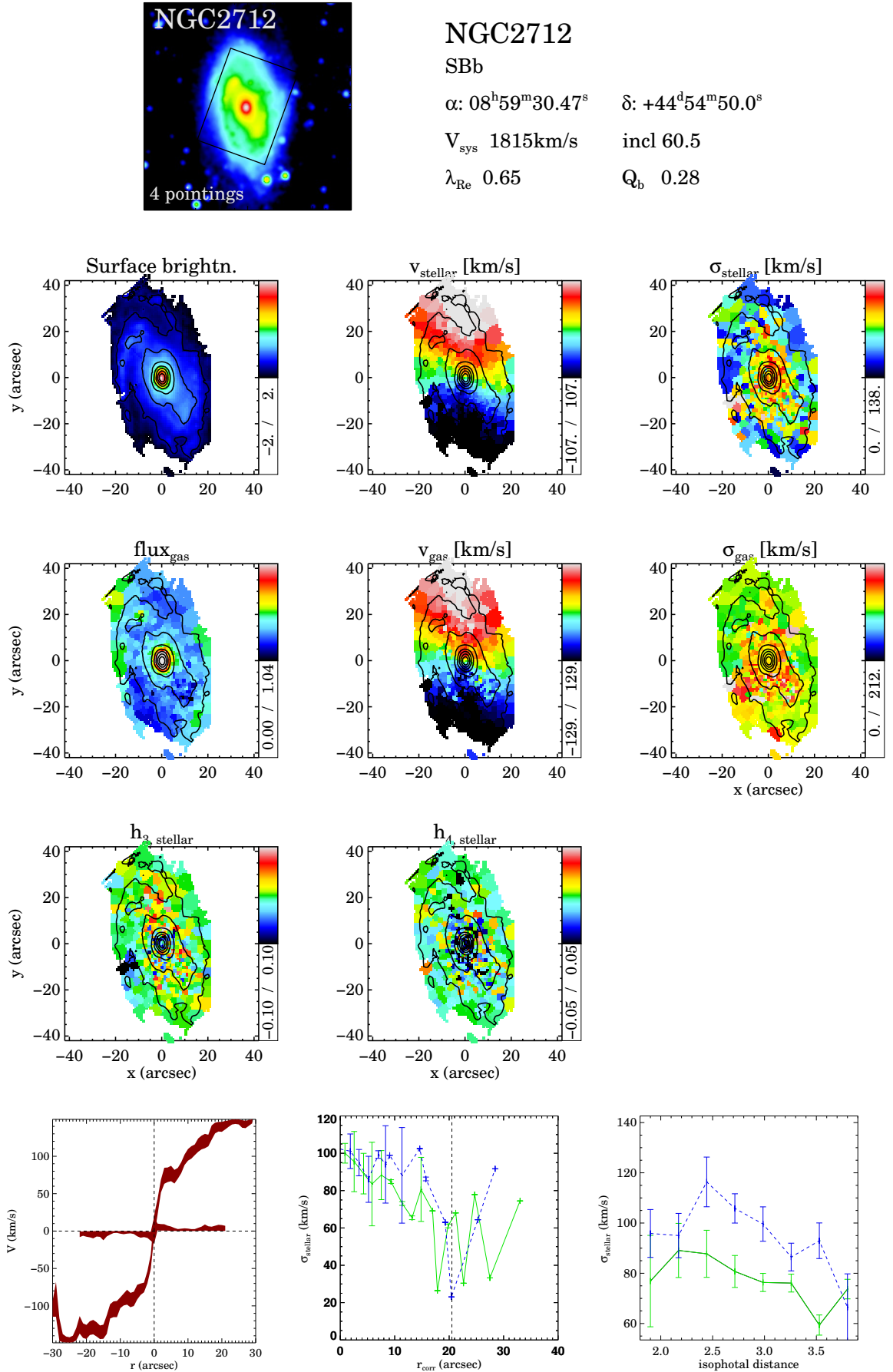


Figure C3. Figure C1 continued.

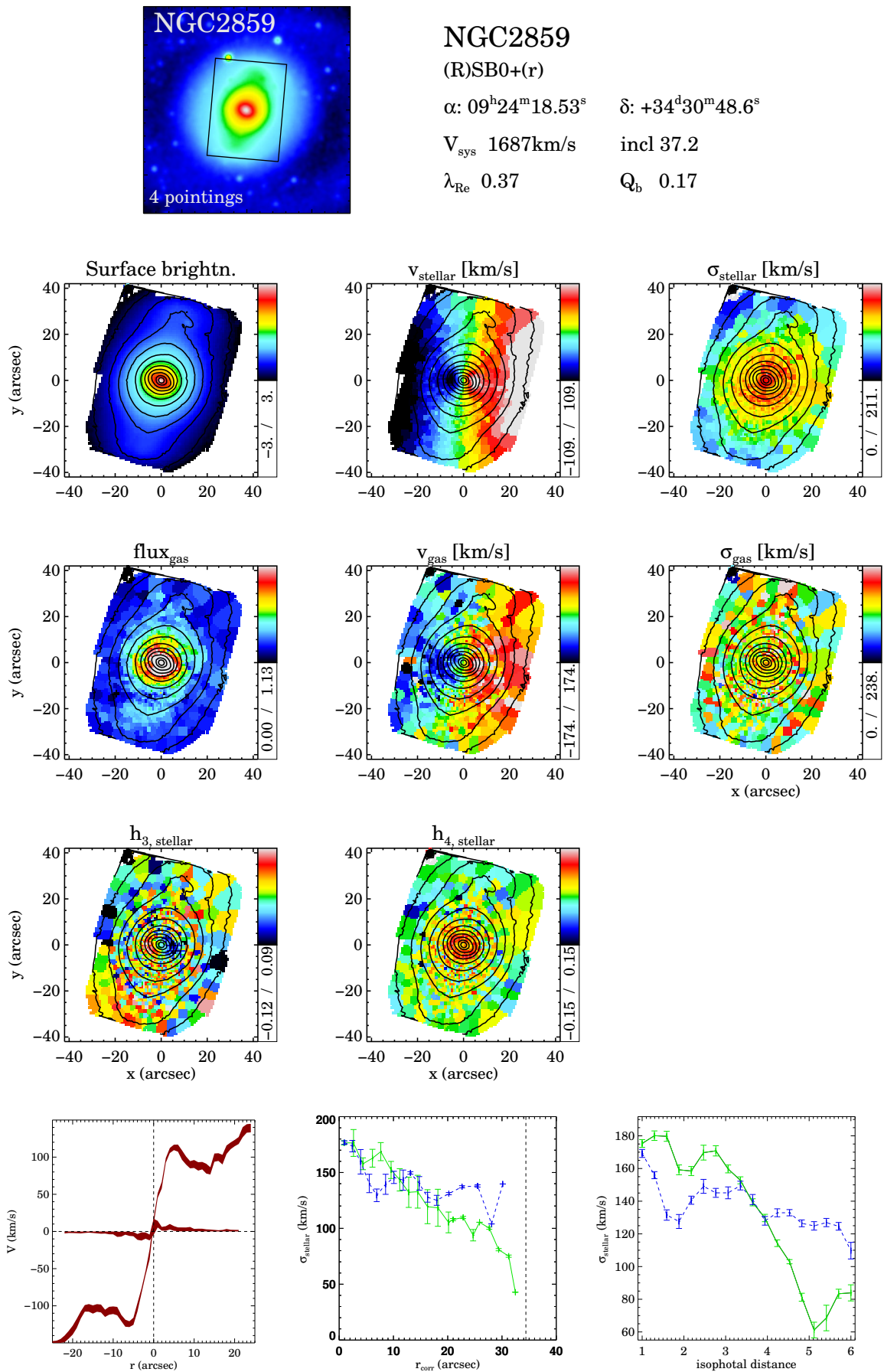


Figure C4. Figure C1 continued.

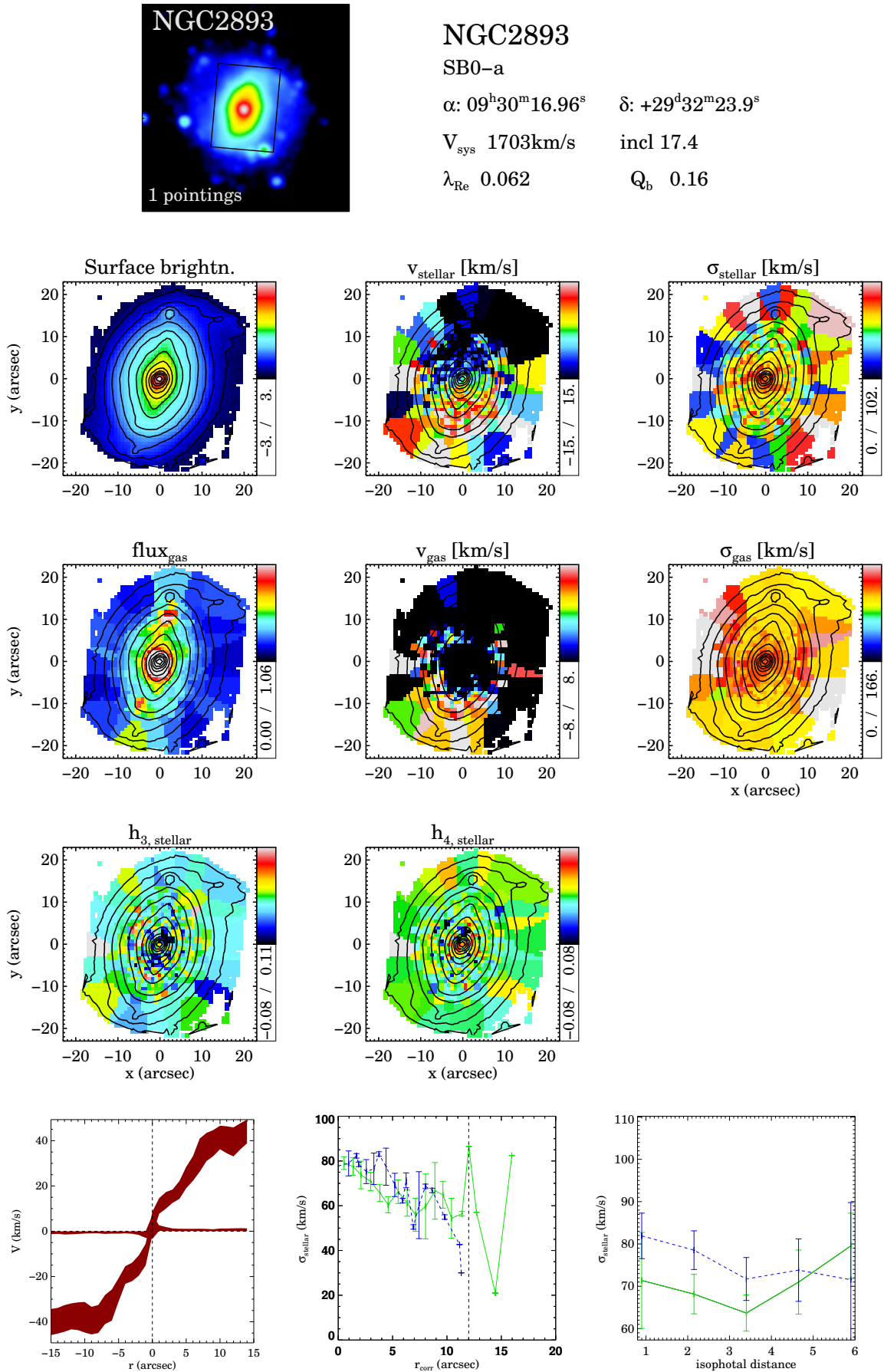


Figure C5. Figure C1 continued.

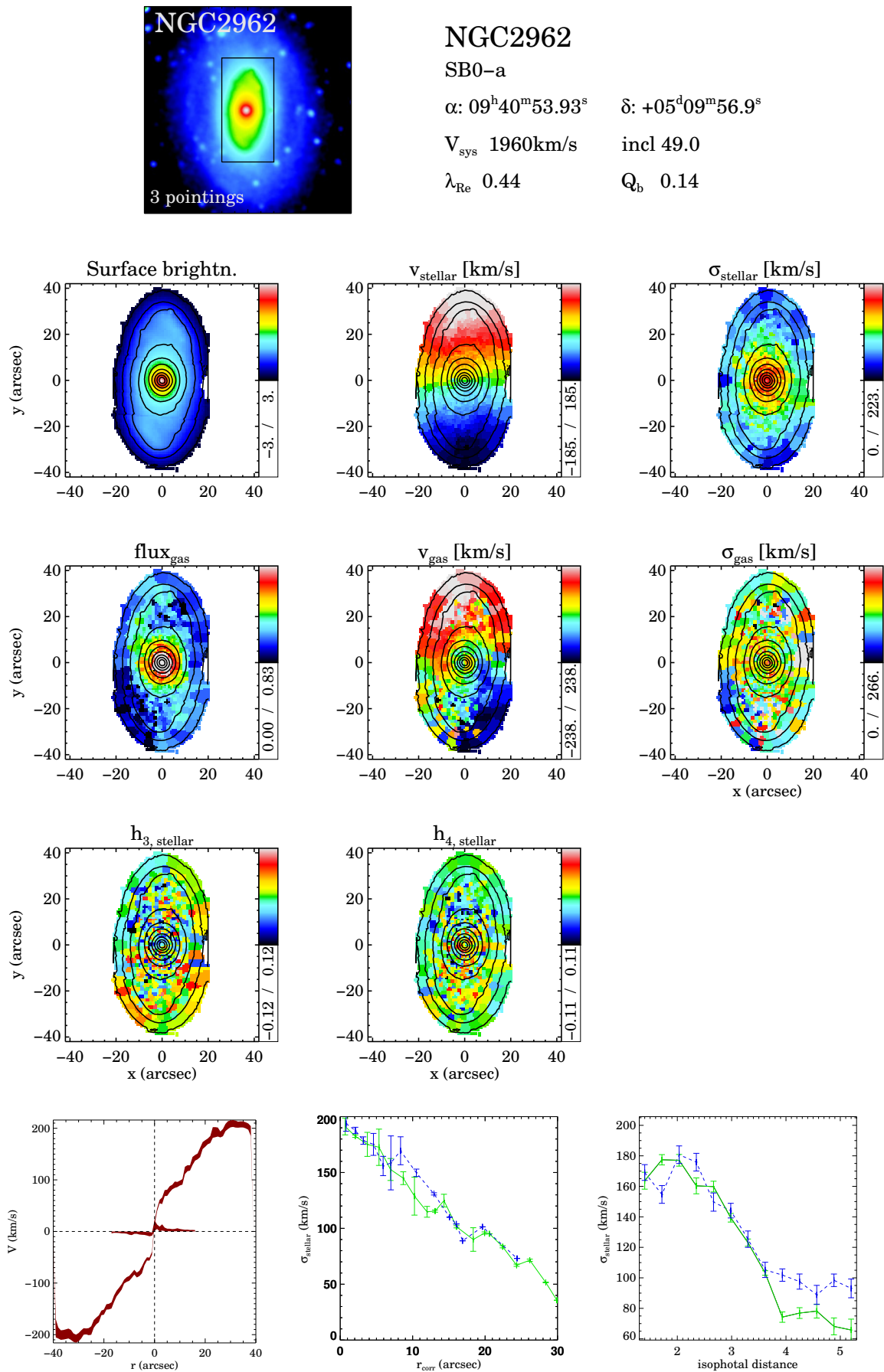
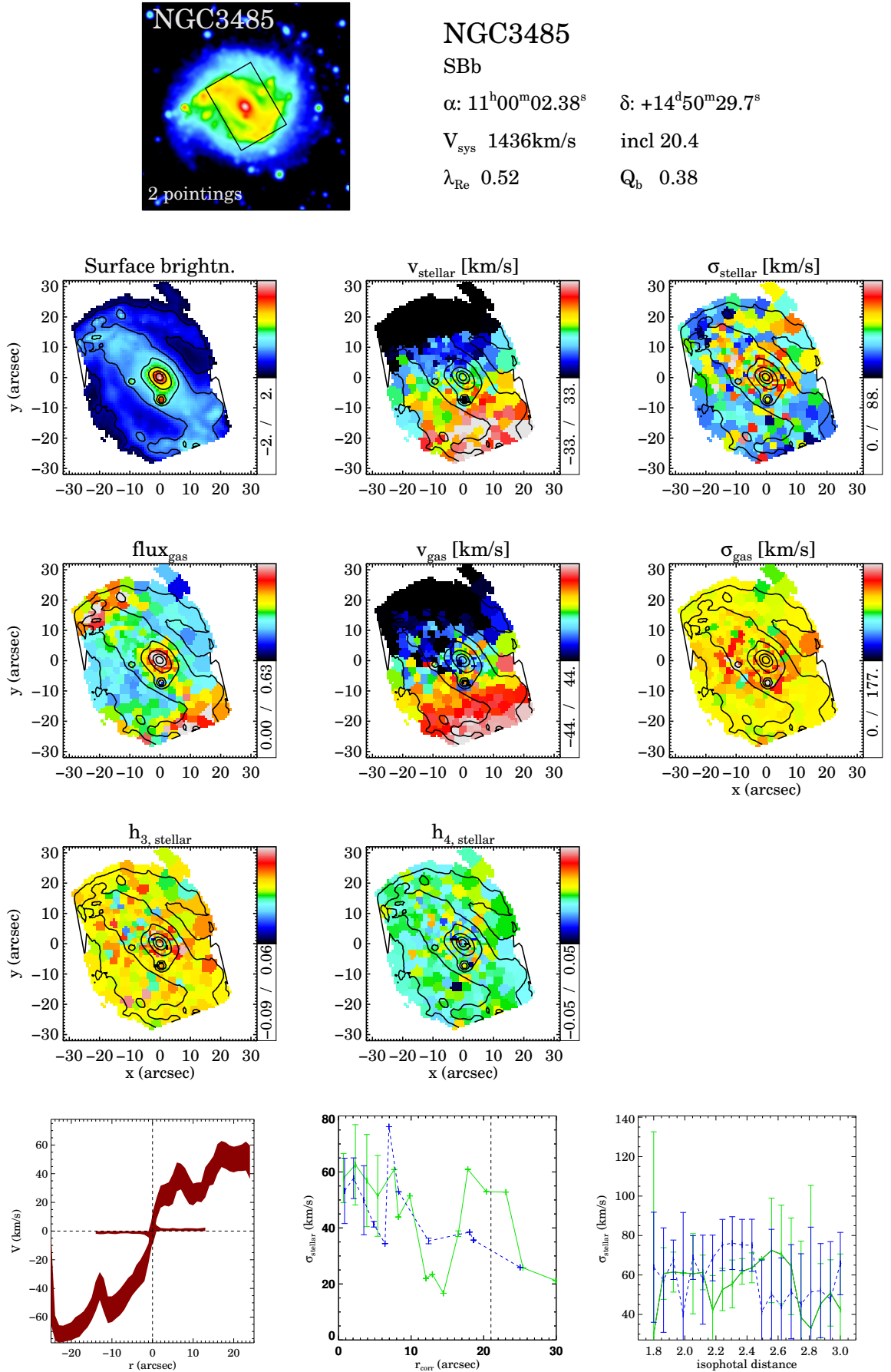
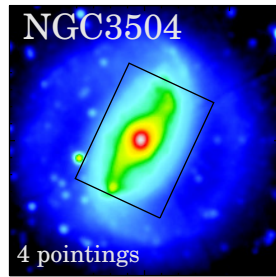


Figure C6. Figure C1 continued.





NGC3504

SBab

α : 11^h03^m11.21^s

δ : +27^d58^m21.0^s

V_{sys} 1539km/s

incl 12.8

λ_{Re} 0.29

Q_b 0.26

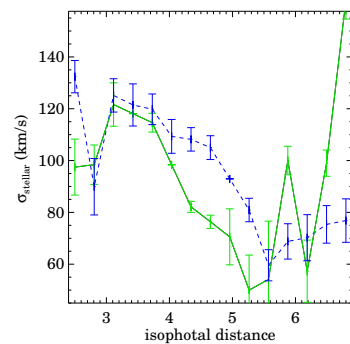
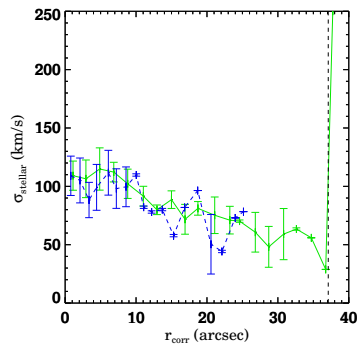
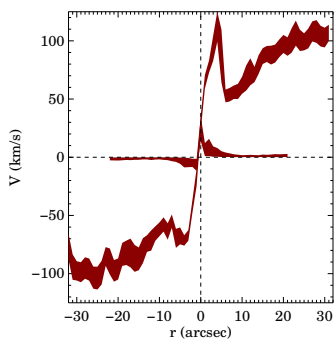
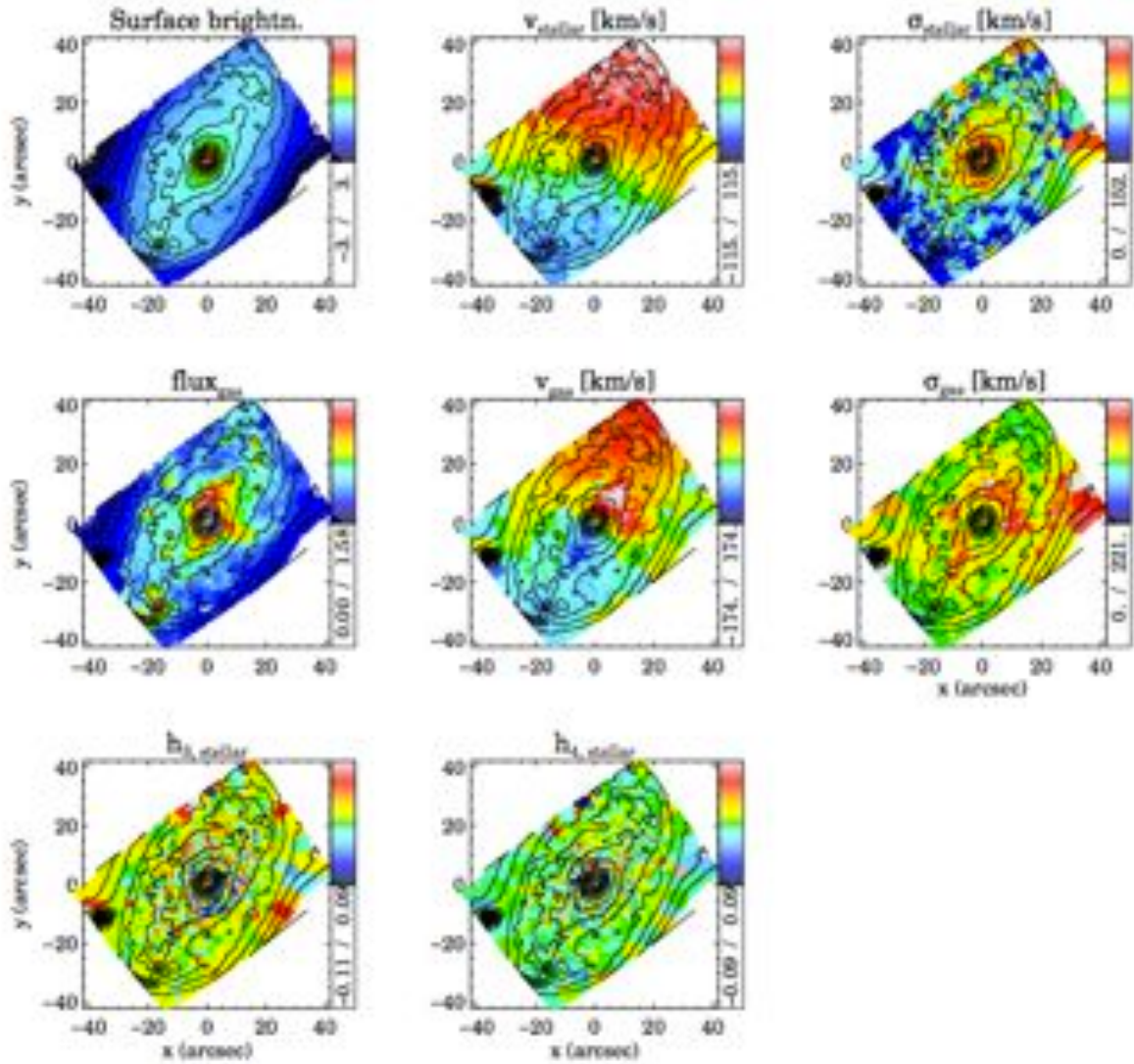
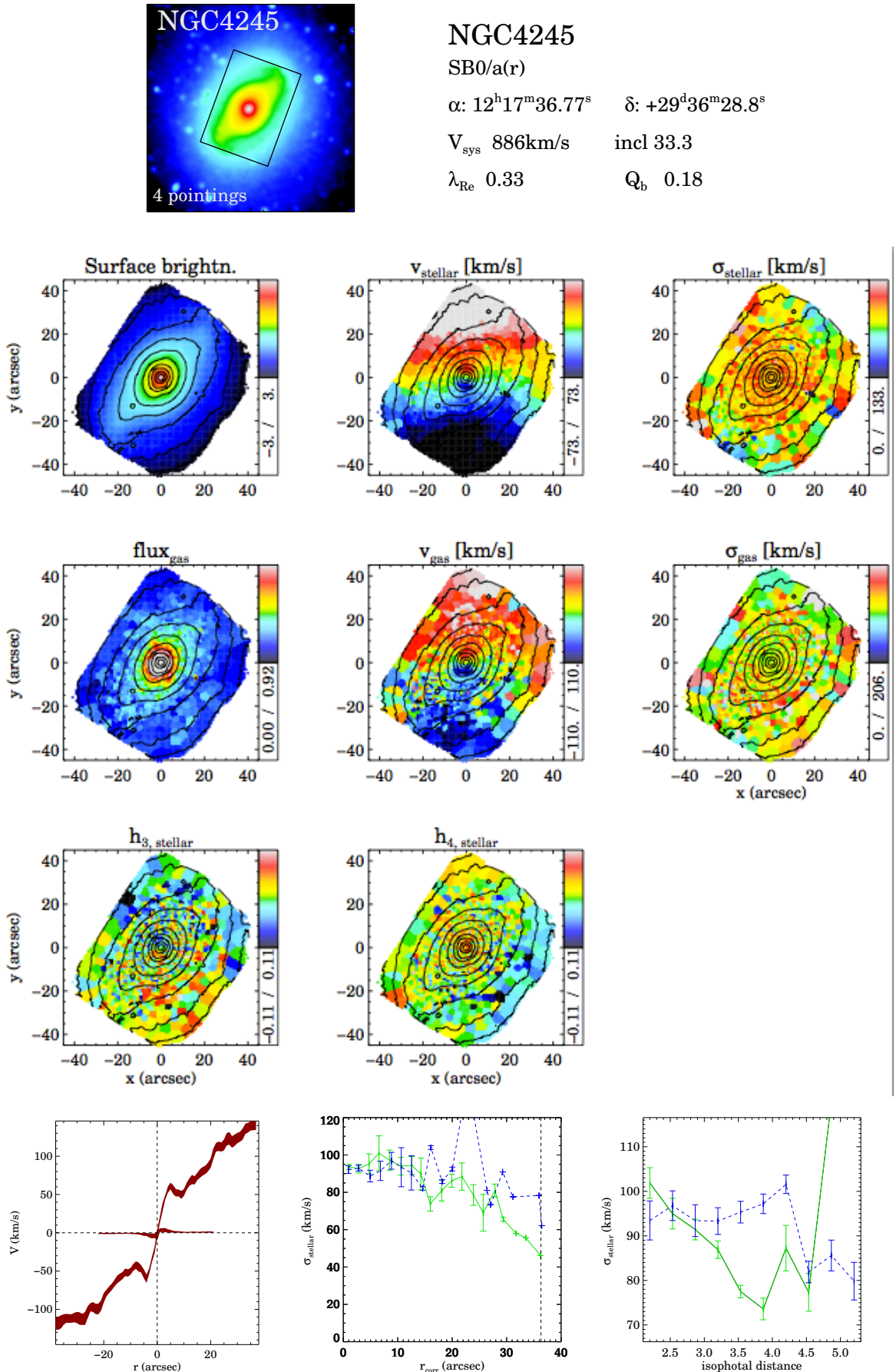


Figure C8. Figure C1 continued.



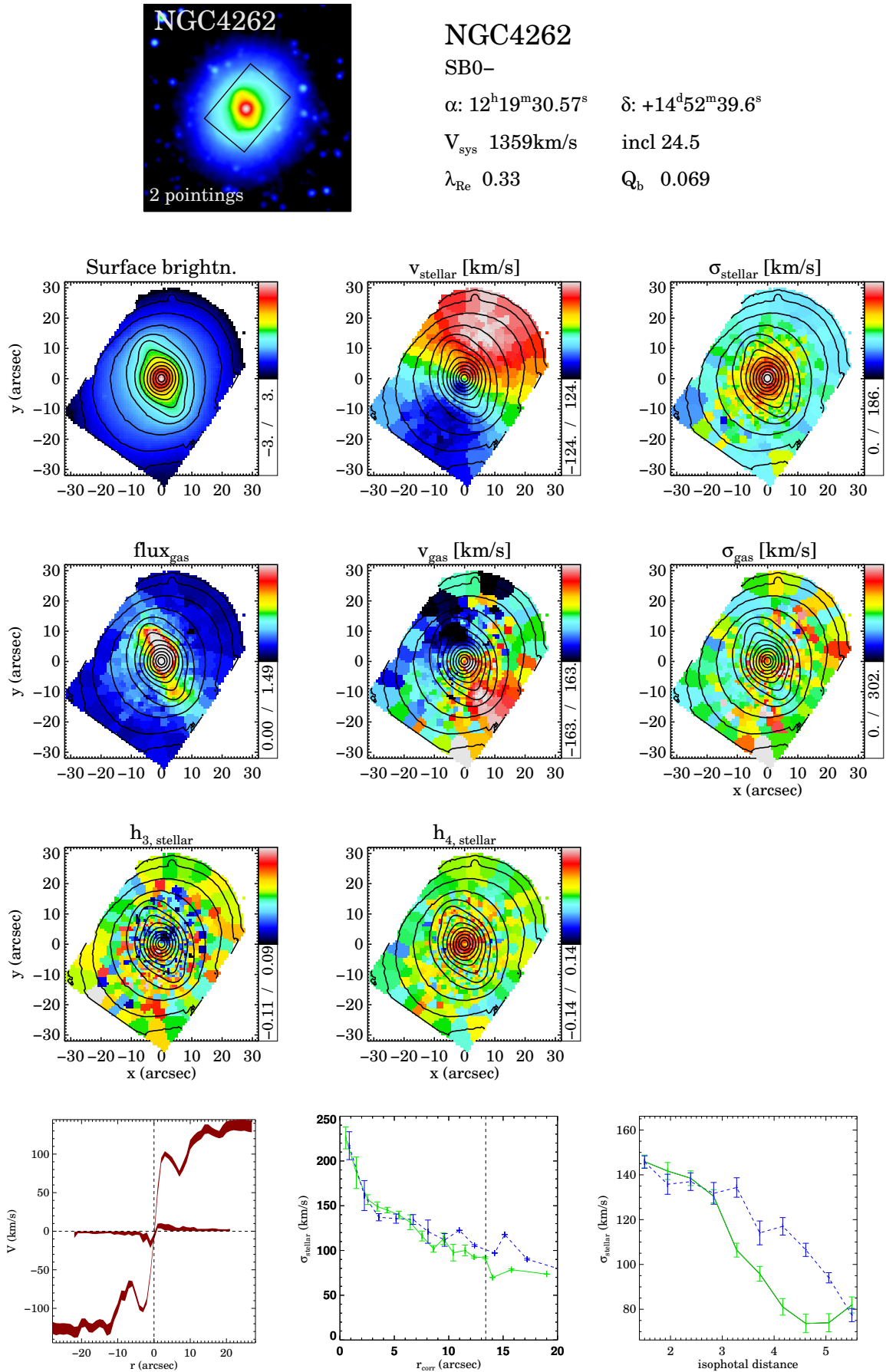
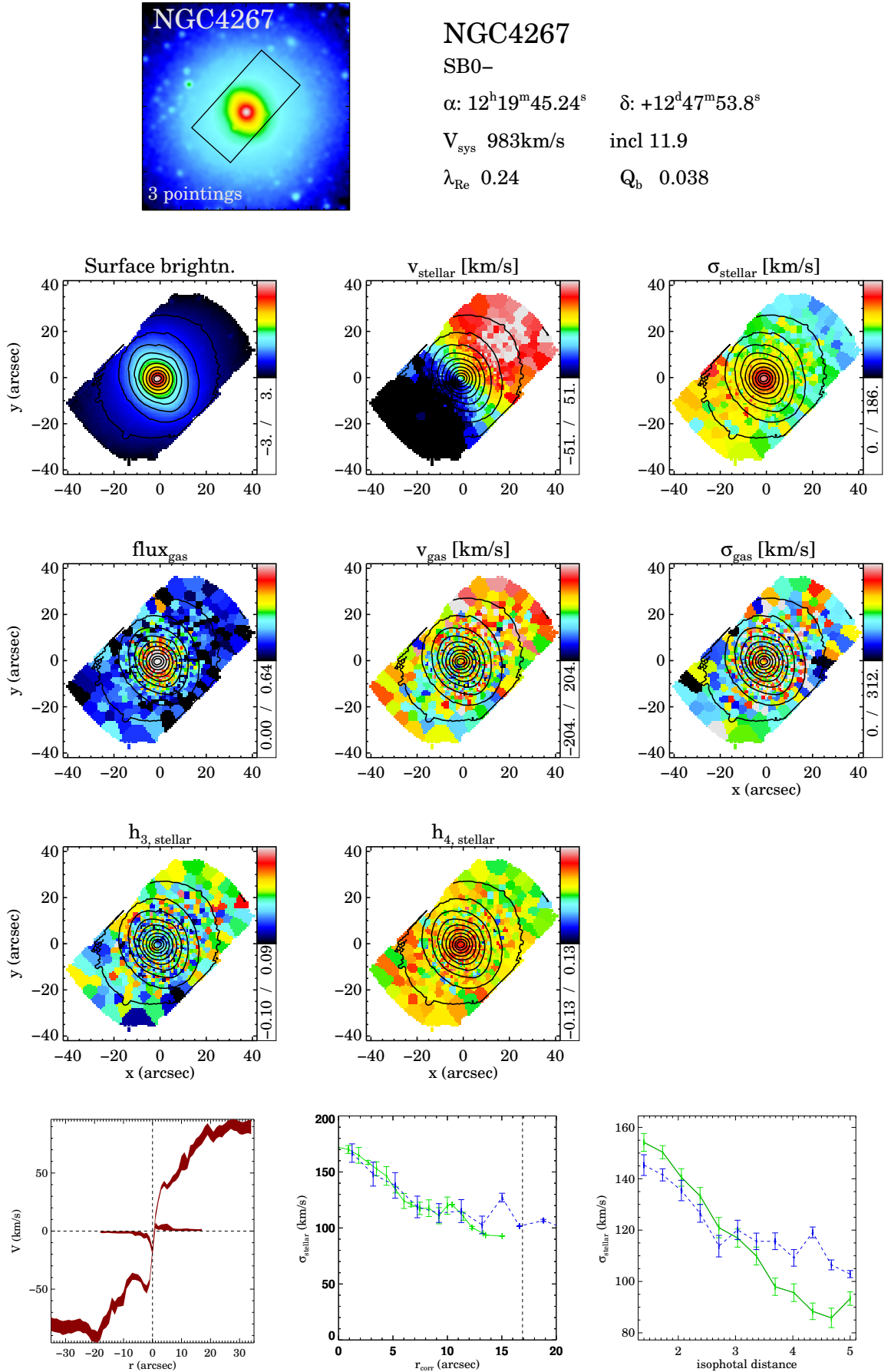


Figure C10. Figure C1 continued.



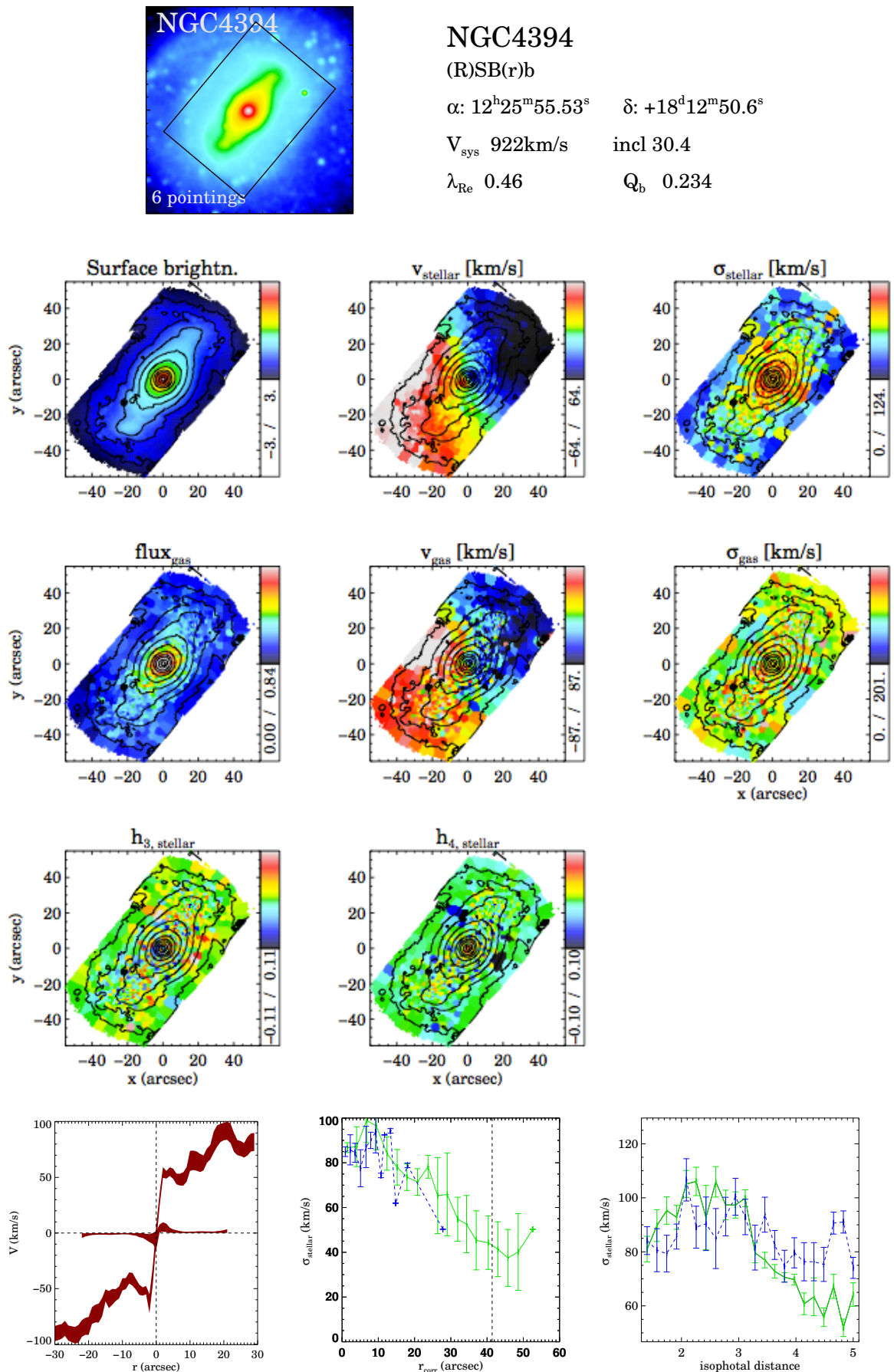


Figure C12. Figure C1 continued.

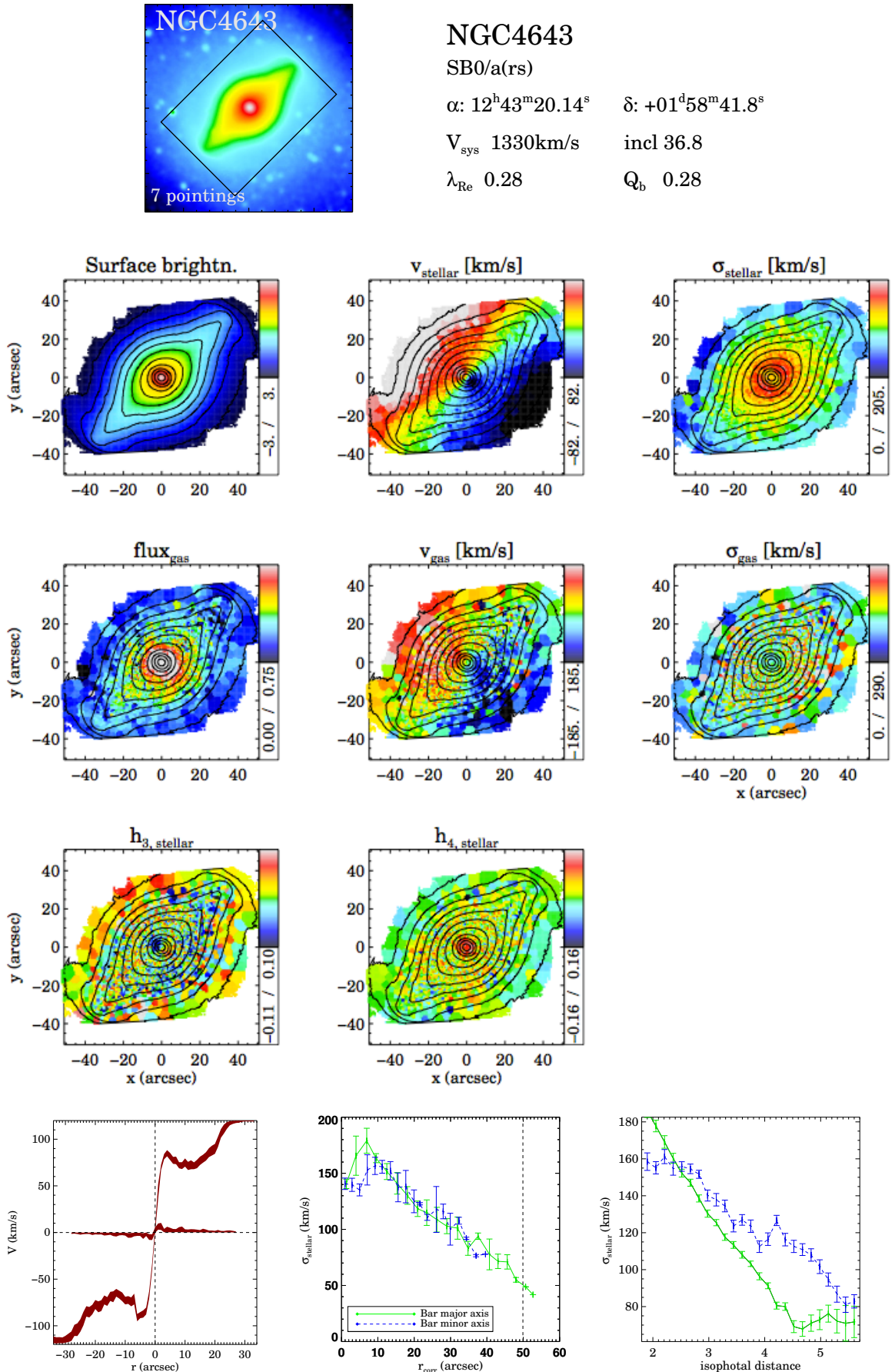


Figure C13. Figure C1 continued.

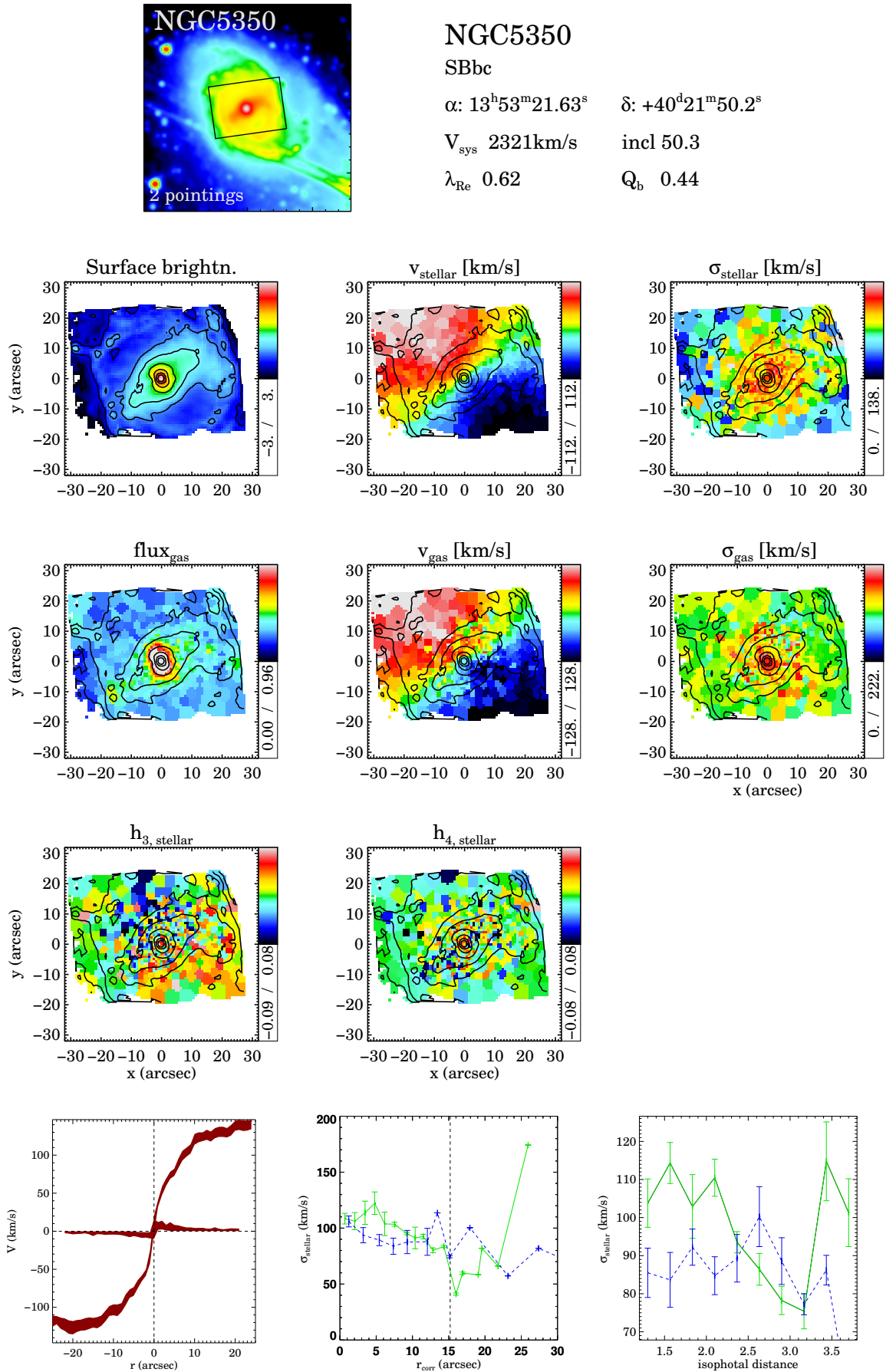
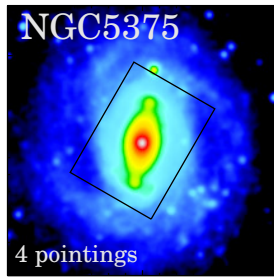


Figure C14. Figure C1 continued.



NGC5375

SBab

α : 13^h56^m56.00^s

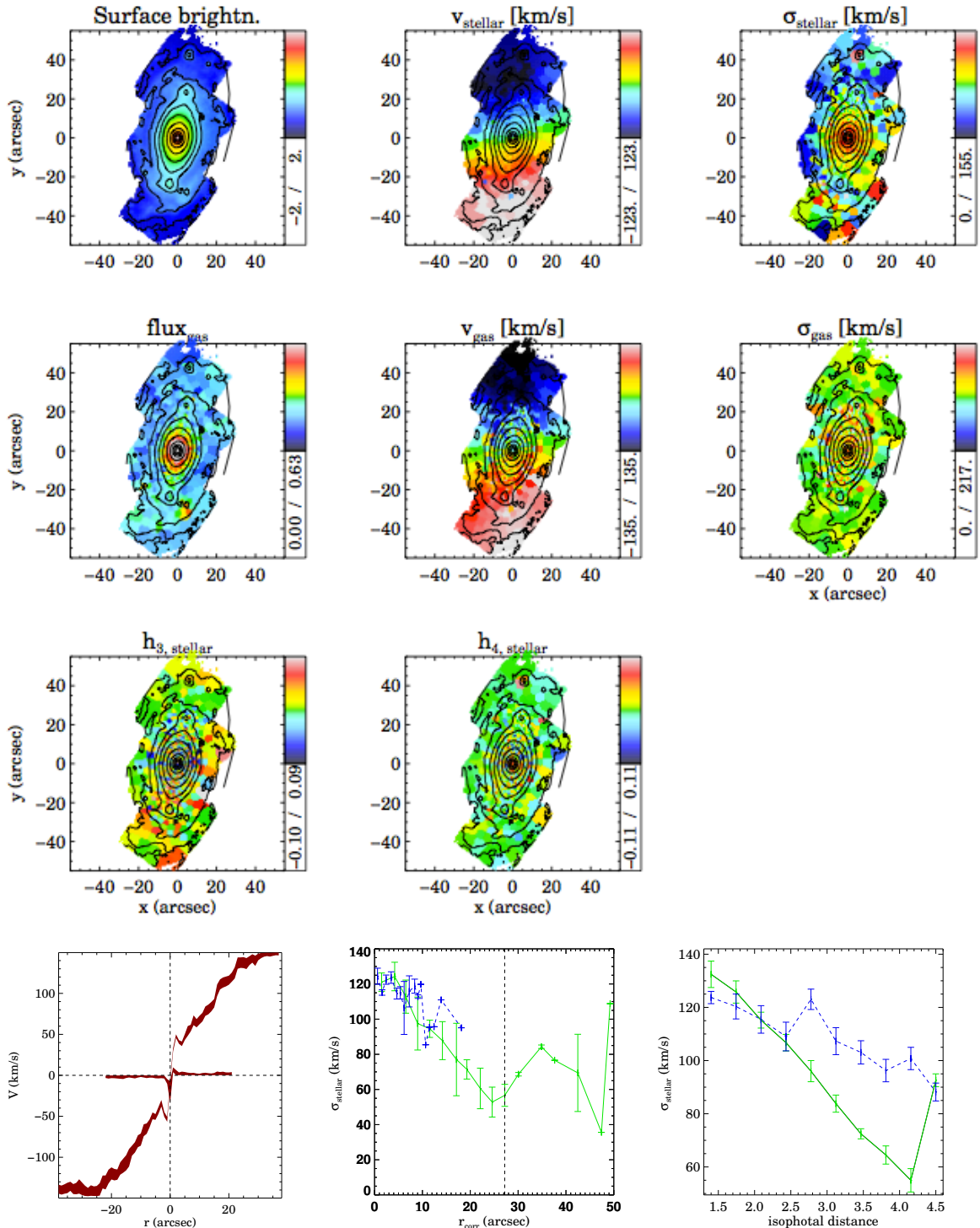
δ : +29^d09^m51.7^s

V_{sys} 2386km/s

incl 29.8

λ_{Re} 0.47

Q_b 0.23



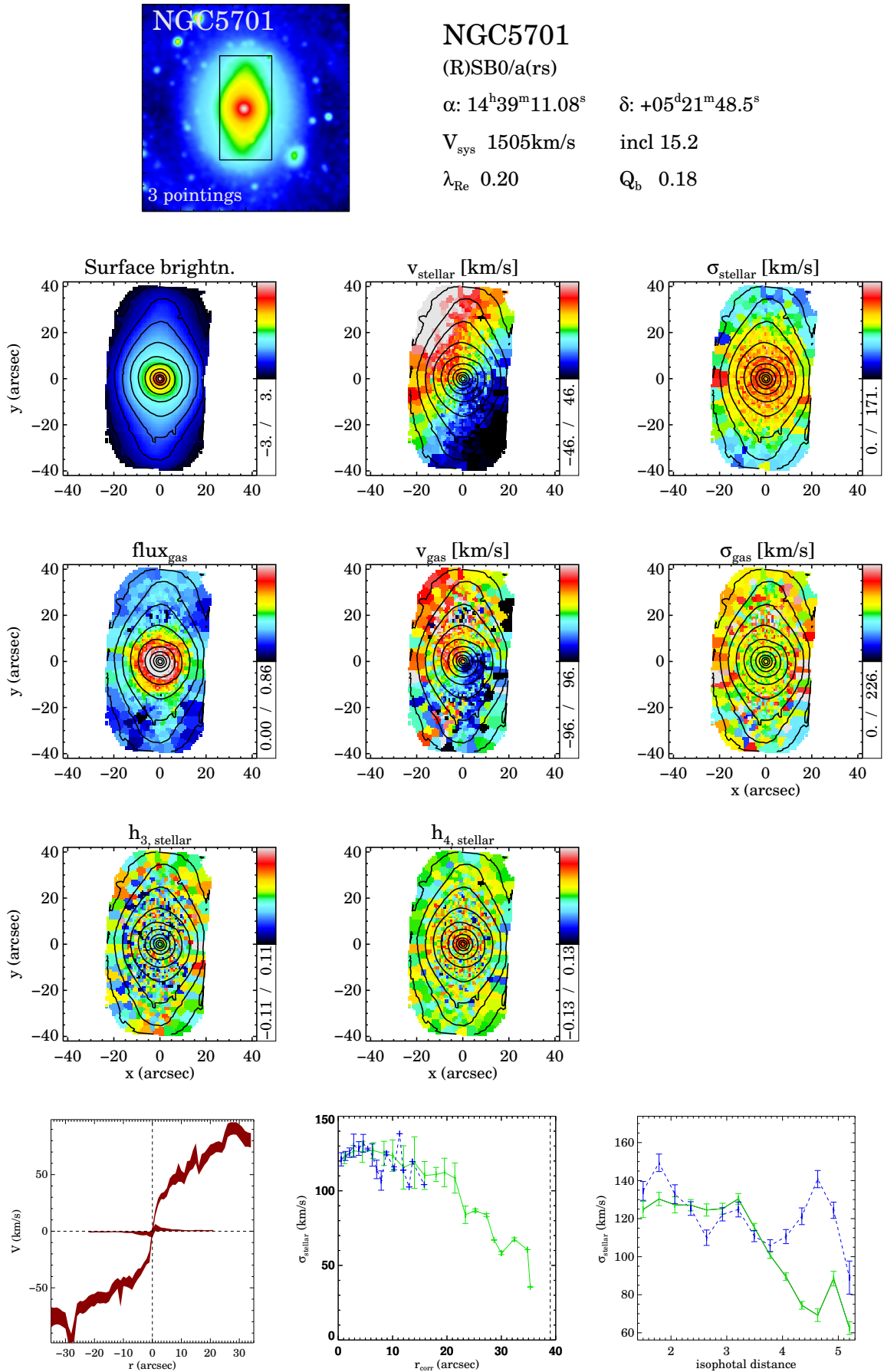


Figure C16. Figure C1 continued.